Variability of Lidar-Derived Particle Properties Over West Africa Due to Changes in Absorption: Towards an Understanding

Igor Veselovskii[1], Qiaoyun Hu[2], Philippe Goloub[2], Thierry Podvin[2], Mikhael Korenskiy[1], Yevgeny Derimian[2], Michel Legrand[2], Patricia Castellanos[3]

[1]*General Physics Institute, Moscow, Russia.*
[2]*Univ. Lille, CNRS, UMR 8518 - LOA - Laboratoire d'Optique Atmospherique, Lille F-59000, France*
[3]*NASA Goddard Space Flight Center, Greenbelt, USA*

Abstract

Measurements performed in Western Africa (Senegal) during the SHADOW-2 field campaign are analyzed to show that spectral dependence of the imaginary part of the complex refractive index (CRI) of dust can be revealed by lidar-measured particle parameters. Observations in April 2015 provide good opportunity for such study, because, due to high optical depth of the dust, exceeding 0.5, the extinction coefficient could be derived from lidar measurements with high accuracy and contribution of other aerosol types, such as biomass burning, was negligible. For instance, in the second half of April 2015, AERONET observations demonstrated a temporal decrease of the imaginary part of CRI at 440 nm from approximately 0.0045 to 0.0025. This decrease is in line with a change in the relationship between the lidar ratios (the extinction-to-backscattering ratio) at 355 nm and 532 nm (S_{355} and S_{532}). For instance in the first half of April, S_{355}/S_{532} is as high as 1.5 and the backscatter Angstrom exponent A_β, is as low as -0.75, while after 15 April $S_{355}/S_{532}=1.0$ and A_β is close to zero. The aerosol depolarization ratio δ_{532} for the whole April exceeded 30% in the height range considered, implying that no other aerosol, except dust, occurred. The performed modeling confirmed that the observed S_{355}/S_{532} and A_β values match the spectrally dependent imaginary part of the refractive index as can be expected for mineral dust containing iron oxides. The second phase of the SHADOW-2 campaign was focused on evaluation of the lidar ratio of smoke and estimates of its dependence on relative humidity (RH). For five studied smoke episodes the lidar ratio increases from 44±5 sr to 66±7 sr at 532 nm and from 62±6 sr to 80±8 sr at 355 nm, when RH varied from 25% to 85%. Performed numerical simulations demonstrate, that observed ratio S_{355}/S_{532}, exceeding 1.0 in the smoke plumes, can indicate to increase of the imaginary part of the smoke particles in the ultraviolet (UV).

1. Introduction

Atmospheric dust provides significant impacts on the Earth's climate system and this impact remains highly uncertain (IPCC report, 2013). In modeling the direct aerosol effect, the vertical profile of the aerosol extinction is one of the basic input parameters, and when this profile

1

37   is derived from the elastic backscatter lidar observations, the knowledge of the extinction-to-
38   backscatter ratio (so called lidar ratio) is essential (Klett, 1985). Although the desert dust in source
39   regions is sometimes qualified as "pure dust", it is always a mixture of various elements, e.g. iron
40   oxides, clays, quartz and calcium–rich species, which proportions can vary (Sokolik and Toon,
41   1999; Wagner et al., 2012; Di Biagio et al., 2017, 2019 and references therein). Thus, the dust
42   optical properties, and hence the lidar ratio (S) can vary, depending on the relative abundance of
43   various minerals in emission sources. The imaginary part of the complex refractive index (CRI) of
44   different minerals can vary spectrally and often exhibits an increase in UV spectral region for dust,
45   containing iron oxides. Therefore, the retrieval of the dust extinction profiles from elastic
46   backscatter lidar observation should account for the spectral variation of the lidar ratio.

47   Raman and HSRL lidars are capable of providing independent profiling of aerosol
48   backscattering and extinction coefficients (Ansmann et al., 1992), and therefore are widely used
49   to measure the lidar ratios of dust from different origins (e.g. Sakai et al., 2003; Papayannis et al.,
50   2008, 2012; Xie et al., 2008; Ansmann et al., 2011; Mamouri et al., 2013; Burton et al., 2014;
51   Nisantzi et al., 2015; Giannakaki et al., 2016; Hofer et al., 2017, 2019; Soupiona et al., 2018,
52   2019). The African deserts are the largest sources of mineral dust and numerous studies have been
53   conducted for quantifying the particle intensive parameters (parameters independent of
54   concentration) during dust transport from this source region to Europe and over the Atlantic Ocean
55   (Mattis et al., 2002; Amiridis et al., 2005; Mona et al., 2006; Papayannis et al., 2008; Preißler et
56   al., 2013; Groß et al., 2015; Rittmeister et al., 2017; Haarig et al. 2017). The dust properties are,
57   however, modified during this transport, experiencing mixing and aging processes, thus the
58   characterization of the dust properties near the source regions is highly important for the evaluation
59   the parameters of "pure dust".

60   The lidar ratios at 355 nm and 532 nm (S_{355} and S_{532}) were measured during the SAMUM-
61   1 and 2 experiments in Morocco and Capo Verde respectively (Esselborn et al., 2009; Tesche et
62   al., 2009, 2011; Groß et al., 2011; Ansmann et al., 2011), as well as during the more recent
63   SHADOW-2 experiment in Senegal (Veselovskii et al., 2016, 2018). The lidar ratios S_{355} and S_{532}
64   measured during SAMUM experiments did not present significant spectral dependence. For
65   example, for SAMUM-2 campaign, the averaged values of S_{355} and S_{532} were 53 ± 10 sr and 54 ± 10
66   sr respectively (Tesche et al., 2011). During SHADOW, however, S_{355} significantly exceeded S_{532}
67   in many dust episodes, which was linked to an increase of the imaginary part of CRI of dust at 355
68   nm (Veselovskii et al., 2016).

69   The dust backscattering coefficient (and so the lidar ratio), in contrast to the extinction
70   coefficient, is sensitive to the imaginary part of CRI (Perrone et al., 2004; Veselovskii et al., 2010;
71   Gasteiger et al., 2011). Thus, it is expected that enhanced absorption in the UV should increase the

72 lidar ratio. In turn, the ratio S_{355}/S_{532} should characterize the spectral variation of the imaginary

73 part of CRI. The latest version of AERONET products (3.0) provides inversions of the lidar related

74 properties, including the lidar ratio, from almucantar scans with ground-based sun photometers.

75 For these products, the shortest available wavelength is 440 nm. Despite the imaginary part at 440

76 nm (Im_{440}) is lower than Im_{355}, AERONET observations still show an increase of absorption at

77 440 nm in respect to 675 nm that yields a ratio of S_{440}/S_{675} close to 1.4 for Saharan dust (Shin et

78 al., 2018). The goal of this work is to analyze the correlation of variations of Im_{440} from

79 AERONET with measured values from lidar to reveal the effect of dust absorption on lidar-derived

80 aerosol properties. We focus on height and day-to-day variations of the dust intensive properties,

81 such as S_{355} and S_{532}, depolarization ratio (δ), as well as the extinction and backscatter Ångström

82 exponents (A_α and A_β respectively) measured during several strong dust episodes in April 2015

83 during the SHADOW-2 campaign.

84   The smoke aerosol particles, typically originated from biomass burning, can also have a

85 pronounced spectral dependence of absorption (Nicolae et al., 2013). This is generally due to

86 presence of carbonaceous particles with organic compounds, so-called brown carbon (BrC) (Sun

87 et al., 2007; Kirchstetter, et al., 2004). The Sahel region is known for seasonal biomass burning

88 caused by human activity on combustion of agricultural waste that can produce an abundant

89 amount of BrC. The smoke can also be mixed with mineral dust during long-range transport or in

90 the emission origin (Haywood et al., 2008). During the SHADOW-2 the observation period

91 included the biomass burning season, thus an additional effort was dedicated to the examination

92 of the spectral lidar ratio variability of transported biomass burning aerosol under different

93 environmental conditions and presents a supplementary subject of the current study.

94   The paper is organized as follows. Section 2 describes the lidar system and provides the

95 main expressions used for the data analysis. Several strong dust episodes, in April 2015, are

96 analyzed in Section 3. In Section 4, the smoke episodes occurring from December 2015 to January

97 2016, are used to evaluate the variation of the smoke lidar ratio with relative humidity. The paper

98 is finalized with conclusion.

99

100   **2. Experimental setup and data analysis**

101   The observations were performed with LILAS multiwavelength Raman lidar during

102 SHADOW-2 campaign at Mbour, Senegal. Information related to the SHADOW-2 and

103 observation site is presented in Veselovskii et al. (2016). The LILAS is based on a tripled Nd:YAG

104 laser with a 20 Hz repetition rate and pulse energy of 90/100/100 mJ at 355/532/1064 nm. The

105 aperture of the receiving telescope is 400 mm. During the campaign, LILAS configuration

106 ($3\beta+2\alpha+1\delta$) allowed the measurement of three particle backscattering (β_{355}, β_{532}, β_{1064}), two

107   extinction coefficients (α_{355}, α_{532}) and depolarization ratio at 532 nm (δ_{532}). To improve the

108   performance of the system at 532 nm the rotational Raman channel was used instead of the

109   vibrational one (Veselovskii et al, 2015). The measurements were performed at a 47 degrees angle

110   to horizon. The backscattering coefficients and depolarization ratios were calculated with a 7.5 m

111   range resolution (corresponding to 5.5 m vertical resolution), while the range resolution of

112   extinction coefficient varied from 50 m (at 1000 m) to 125 m (at 7000 m). Particle extinction and

113   backscattering coefficients at 355 nm and 532 nm are calculated from elastic and Raman

114   backscatter signals, as described in Ansmann et al. (1992) and corresponding uncertainties are

115   shown on the plots. An additional Raman reception channel at 408 nm was setup for profiling the

116   water vapor mixing ratio (WVMR) (Whiteman et al., 1992).

117   The particle depolarization ratio δ, determined as a ratio of cross- and co-polarized

118   components of the particle backscattering coefficient, was calculated and calibrated the same way

119   as described in Freudenthaler et al. (2009). The relative uncertainty of depolarization

120   measurements due to calibration is estimated as ±10%. To analyze the complex aerosol mixtures,

121   containing dust (d) and smoke (s), we can write $\beta = \beta^d + \beta^s$ and $\alpha = \alpha^d + \alpha^s$. The depolarization

122   ratio of such a mixture is therefore:

123
$$\delta = \frac{\left(\dfrac{\delta^d}{1+\delta^d}\right)\beta^d + \left(\dfrac{\delta^s}{1+\delta^s}\right)\beta^s}{\dfrac{\beta^d}{1+\delta^d} + \dfrac{\beta^s}{1+\delta^s}} \tag{1}$$

124   Here δ^d and δ^s are the particle depolarization ratios of dust and smoke components respectively.

125   To characterize the spectral dependence of the extinction (α) and backscattering (β)

126   coefficients, the corresponding Ångström exponents are introduced as:

127
$$A_\alpha = \frac{\ln\left(\dfrac{\alpha_{\lambda_1}}{\alpha_{\lambda_2}}\right)}{\ln\left(\dfrac{\lambda_2}{\lambda_1}\right)} \quad \text{and} \quad A_\beta = \frac{\ln\left(\dfrac{\beta_{\lambda_1}}{\beta_{\lambda_2}}\right)}{\ln\left(\dfrac{\lambda_2}{\lambda_1}\right)} \tag{2}$$

128   Where α_{λ_1}, α_{λ_2}, β_{λ_1}, β_{λ_2} are the extinction and backscattering coefficients at wavelengths λ_1 and

129   λ_2. For the mixture of smoke and dust, the extinction Ångström exponent (EAE) can be calculated

130   from the ratio $\dfrac{\alpha_{\lambda_1}}{\alpha_{\lambda_2}}$:

131
$$\frac{\alpha_{\lambda_1}}{\alpha_{\lambda_2}} = \frac{\alpha_{\lambda_1}^d + \alpha_{\lambda_1}^s}{\alpha_{\lambda_2}^d + \alpha_{\lambda_2}^s} = \frac{\alpha_{\lambda_1}^d}{\alpha_{\lambda_2}^d} \frac{\left(1 + \frac{\alpha_{\lambda_1}^s}{\alpha_{\lambda_1}^d}\right)}{\left(1 + \frac{\alpha_{\lambda_2}^s}{\alpha_{\lambda_2}^d}\right)} = \frac{\alpha_{\lambda_1}^d}{\alpha_{\lambda_2}^d} \frac{\left(1 + \frac{\alpha_{\lambda_2}^s (\frac{\lambda_2}{\lambda_1})^{A_\alpha^s}}{\alpha_{\lambda_2}^d (\frac{\lambda_2}{\lambda_1})^{A_\alpha^d}}\right)}{\left(1 + \frac{\alpha_{\lambda_2}^s}{\alpha_{\lambda_2}^d}\right)} = \frac{\alpha_{\lambda_1}^d}{\alpha_{\lambda_2}^d} \frac{\left(1 + \frac{\alpha_{\lambda_2}^s}{\alpha_{\lambda_2}^d}\left(\frac{\lambda_2}{\lambda_1}\right)^{(A_\alpha^s - A_\alpha^d)}\right)}{\left(1 + \frac{\alpha_{\lambda_2}^s}{\alpha_{\lambda_2}^d}\right)}$$ (3)

132 Here A_α^d and A_α^s are the Ångström exponents of dust and smoke. The Ångström exponent of the

133 mixture is obtained from (3):

134
$$A_\alpha = \frac{\ln\frac{\alpha_{\lambda_1}}{\alpha_{\lambda_2}}}{\ln\frac{\lambda_2}{\lambda_1}} = A_\alpha^d + \frac{1}{\ln\frac{\lambda_2}{\lambda_1}} \ln\left[\frac{\left(1 + \frac{\alpha_{\lambda_2}^s}{\alpha_{\lambda_2}^d}\left(\frac{\lambda_2}{\lambda_1}\right)^{(A_\alpha^s - A_\alpha^d)}\right)}{\left(1 + \frac{\alpha_{\lambda_2}^s}{\alpha_{\lambda_2}^d}\right)}\right]$$ (4)

135 The backscattering Ångström exponent (BAE) can be calculated in a similar way. And finally, the

136 lidar ratio of the aerosol mixture is calculated as:

137
$$S = \frac{S^d \beta^d + S^s \beta^s}{\beta^d + \beta^s} = S^d + \frac{\beta^s}{\beta}(S^s - S^d)$$ (5)

138 where S^d and S^s are the lidar ratios of dust and smoke.

139

140 **3. Dust observations in March and April 2015**

141 The aerosol over West Africa presents strong seasonal variations. The spring is

142 characterized by strong dust emission, while, during winter season, intense forest fires occurring

143 in the equatorial regions emit smoke particles that are transported over Senegal (Veselovskii et al.,

144 2018). The SHADOW-2 campaign included the following periods of measurements: 13 March –

145 25 April 2015, 8–25 December 2015 and 5-24 January 2016, so numerous dust and smoke episodes

146 were observed. In our analysis of lidar-derived aerosol properties, we considered also aerosol

147 columnar properties provided by AERONET (Holben et al. 1998) and aerosol profiles predicted

148 by the Modern-Era Retrospective analysis for Research and Applications, Version 2 (MERRA-2)

149 aerosol reanalysis (Gelaro et al., 2017; Randles et al., 2017). MERRA-2 is the first long-term

150 global reanalysis to assimilate space-based aerosol observations and include their radiative

151 coupling with atmospheric dynamics. MERRA-2 is driven by the Goddard Earth Observing

152 System (GEOS) model version 5 that includes the Goddard Chemistry, Aerosol, Radiation and

153 Transport (GOCART) module. GOCART models the sources, sinks, and transformation of the

154 following five aerosol species as external mixtures: dust, organic carbon (OC), black carbon (BC),

155 sulfates (SU) and sea salt (SS). Dust and sea salt are represented by five non-interacting size bins,

156   and have wind-speed dependent emissions. The MERRA-2 reanalysis assimilates AOD
157   observations from the twin Moderate Resolution Imaging Spectroradiometer (MODIS)
158   instruments, MODIS-Terra and MODIS-Aqua, as well as the AERONET ground-based sun
159   photometer network. In addition, the profiles of meteorological variables (P, T, RH), provided by
160   radio-sondes at the Dakar airport, located ~70 km from the M'bour site, were also available. The
161   relative humidity (RH) profiles over the M'bour site were calculated from the combination of lidar-
162   derived WVMR and temperature profile from radiosounding.

163   Fig.1 shows the aerosol optical depth at 532 nm (AOD_{532}) for March, April and December
164   2015 recalculated from AERONET AOD at 500 nm using the 440-675 nm Ångström exponent.
165   The same figure shows the AODs for the five aerosol species used in MERRA-2 model, such as
166   dust, organic carbon (OC), black carbon (BC), sulfates (SU) and sea salt (SS). The optical depths
167   provided by MERRA-2 and AERONET are in a good agreement. Dust is the predominant aerosol
168   component for all three months with the highest values of AOD in April. The contribution of
169   organic carbon (the main component of the biomass burning products) is significant in December,
170   when the forest fire season starts in equatorial regions, though noticeable amount of OC is
171   predicted also for March and for the beginning of April. The contribution of BC and SU to the
172   total AOD is low: the sum of the corresponding AODs is below 0.1 for all three months.

173   The single scattering albedo (SSA) over the M'Bour site in 2015 provided by AERONET
174   at 440 and 675 nm is shown in Fig.2. The SSA_{675} is above 0.97 for March – April period, but at
175   440 nm dust absorption is stronger and, in March, SSA_{440} is about 0.9. However, in the middle of
176   April, SSA_{440} increases up to 0.95, indicating that aerosols become less absorbing at shorter
177   wavelengths. We can thus expect that variation of SSA at 355 nm between April and March should
178   be even stronger. In our study we consider two groups of observations. The first group corresponds
179   to the beginning of April, when SSA at 440 nm was lower. The second group covers the second
180   half of April, when SSA at 440 nm increased. By analyzing these two groups we expect to reveal
181   the effect of aerosol absorption, on lidar-derived aerosol properties.

182

183   **3.1. Dust episode on 1 – 4 April 2015**

184   In the beginning of April the dust was transported by Continental trades (Harmattan) from
185   the northeastern/eastern drylands. For period 1 - 4 April, as follows from Fig.1b, the AOD_{532} over
186   Dakar increased up to 1.0. Fig.3 shows the spatio-temporal distributions of the aerosol
187   backscattering coefficient β_{532}, particle depolarization ratio δ_{532}, and water vapor mixing ratio for
188   the nights 1-2, 2-3 and 3-4 April 2015. The corresponding airmass back-trajectories, shown in
189   Fig.4, demonstrate that, on 1-2 and 2-3 April, air masses at all heights arrive from the North-East,
190   whereas on 3-4 April the air masses above 2500 m are advected from the East. These air masses

191   are characterized by higher humidity and may contain biomass-burning products. During these
192   three nights, the linear particle depolarization ratio and WVMR present some evolution. On 1-2
193   April δ_{532} exceeds 30% and does not change significantly within the dust layer, even if some
194   decrease is observed above 2000 m after 03:00 UTC. By 3-4 April the depolarization ratio above
195   2500 m decreases below 25%, simultaneously with increase of the WVMR. During the dust
196   episode, the relative humidity did not exceed 20% on 1-3 April, but on 3-4 April it increased up to
197   40% above 2500 m.

198   Vertical profiles of dust particle properties such as aerosol extinction coefficients α_{355}, α_{532},
199   particle depolarization ratio δ_{532} and lidar ratios S_{355}, S_{532} are shown on Fig.5 for the three
200   observation periods on 1, 2-3 and 3-4 April 2015. The profiles of backscattering coefficients for
201   2-3 and 3-4 April are given by Fig.6, while the extinction and backscatter Ångström exponents,
202   calculated at 355 and 532 nm wavelengths for three temporal intervals from Fig.5, are presented
203   in Fig.7. During all three observation periods A_α is slightly negative ($A_\alpha = -0.1\pm0.1$) up to 2000 m.
204   For the dust component, MERRA-2 provides value of $A_\alpha = -0.14$, which agrees with observations.
205   Above 2000 m, A_α exhibits some increase, which is most significant on 3-4 April, when A_α reaches
206   0.3 ± 0.1 at 4000 m height. Simultaneous decrease of δ_{532} indicates to the possible presence of
207   smoke particles above 2000 m. The backscatter Ångström exponent A_β, in contrast with A_α, is
208   sensitive to the spectral dependence of the imaginary part of CRI, thus yielding complicated
209   vertical variability of A_β. In particular, on 2-3 April A_β decreases from -0.5 to -0.7 within 1500–
210   2500 m height range, when A_α remains stable.

211   As follows from Fig.5, on 1 April the lidar ratio $S_{355}=70\pm6$ sr does not change with height,
212   while S_{532} gradually decreases from 60 ± 5 sr at 1000 m to 50 ± 4 sr at 3000 m height. On sessions
213   that followed (Fig.5b,c) the lidar ratios at both 355 nm and 532 nm decreased. Thus, the range of
214   lidar ratios variation for the dust episode on 1-4 April is 60-70 sr at 355 nm and 45-60 sr at 532
215   nm. The lidar ratios (S_{355} and S_{532}) modeled by MERRA-2 for the dust component are also shown
216   on Fig. 5. The corresponding lidar ratio values are of 70 sr and 42 sr respectively and do not vary
217   with altitude as the model optical properties of all dust size bins based on spectral complex
218   refractive indices from the Optical Properties of Aerosols and Clouds (OPAC) tables (Hess et al.
219   1998) and the spheroidal shape models developed by Meng et al. (2010) are the same and fixed,
220   as dust is treated as hydrophobic. Modeled value S_{355} is near the top of the range of observed
221   values, while modeled S_{532} underestimates the observations.

222   The gradual decrease of S_{532} with height in Fig.5a,c is however unusual. There are, at least,
223   two possible reasons to explain S_{532} height variation. The first one can be the presence of non-dust
224   particles, for example, smoke. The second reason is that the properties (composition) of dust

7

225 change with height. If non-dust particles are present, the particle intensive properties, such as S, δ
226 and A_α should vary with height in consistent way. The MERRA-2 modeling reported in Fig.1
227 shows that in the beginning of April the organic carbon is the second main contributor to the AOD,
228 after dust. We should recall, however, that the model can provide a realistic range of OC variation,
229 however not necessarily reproducing the exact spatio-temporal distribution of OC extinction
230 coefficient.

231   In the dust episode considered, the most significant smoke contribution was observed on
232 3-4 April. Fig.8a shows the profiles of measured α_{355} and α_{532} together with MERRA-2 modeled
233 extinction coefficients at 532 nm for five aerosol components. The extinction Ångström exponents
234 measured by lidar and modeled by MERRA-2 for dust component are given by Fig.8b. The same
235 figure shows also the lidar derived water vapor mixing ratio profile together with the relative
236 humidity. At low altitudes (below 2500 m), where aerosol is represented by pure dust, the
237 measured and modeled values of extinction coefficients are close. Above 2500 m the measured
238 value of α_{355} exceeds that of α_{532}, indicating the presence of smoke particles, while modeled
239 contribution of OC to the total extinction is very low. The measured extinction Ångström exponent
240 is about -0.1 below 2000 m, which well agrees with modeling results for pure dust. Increase of
241 WVMR and RH above 2000 m coincides with growth of the A_α. For the considered case, the
242 model reproduces correctly the dust loading, but underestimates the smoke contribution. At 3500
243 m, the difference between measured and modeled α_{532} is about 0.045 km^{-1} which can be attributed
244 to the smoke contribution.

245   Dust and smoke particles contributions to the total backscattering coefficient can be also
246 separated on the basis of the depolarization measurements, assuming that depolarization ratios of
247 these particles are known (Tesche et al., 2009). The results of such decomposition are presented
248 in Fig.8c, assuming 35% and 7% for dust and smoke depolarization ratio. The δ_{532}=7% was the
249 lowest value that we observed in elevated smoke layers during the SHADOW experiment
250 (Veselovskii et al., 2018), however, due to large difference of smoke and dust depolarization ratios,
251 the choice of exact value for the smoke did not influence significantly the results. The contribution
252 of smoke to the total β_{532} at 3500 m is 0.0009 km^{-1}sr^{-1}. For the smoke lidar ratio of 50 sr at 532 nm
253 (validity of this choice will be discussed in section 3.3), the smoke extinction coefficient is about
254 0.045 km^{-1}. This value agrees well with smoke contribution obtained from Fig.8a at 3500 m and
255 thus can be used for estimating the smoke effect on the intensive aerosols properties derived from
256 lidar measurements.

257   The depolarization ratio of the "dust-smoke" mixture, calculated with expression (1),
258 matches the observed value since decomposition in Fig.8c is based on depolarization

8

259 measurements. The Ångström exponent at 3500 m computed with (4) for α_{532}^{s} =0.045 km^{-1}, α_{532}^{d}

260 =0.147 km^{-1}, A_{α}^{d}=-0.1 and A_{α}^{s}=0.9 yields A_{α} =0.28, which is close to observed value 0.26±0.08.

261 Hence, the observed variation of A_{α} above 2000 m on 3-4 April is well explained by smoke

262 contribution. In a similar way, using (5) we can estimate the smoke lidar ratio (S_{532}^{s}) that would

263 match the observed decrease of S_{532}. To explain decrease of the lidar ratio at 3500 m from 50 sr

264 to 45 sr, the smoke lidar ratio should be about 25 sr, which is unrealistically small (Burton et al.,

265 2012). Such small lidar ratio could be attributed to the maritime aerosol, but then the lidar ratios

266 at both wavelengths should decrease simultaneously. Recall that on 1-2 April smoke contribution

267 was significantly lower, while decrease of S$_{532}$ is about 10 sr. Thus, smoke particles presence

268 cannot explain the observed decrease of S$_{532}$ and it should be probably attributed to changes of

269 dust composition (and so the imaginary part) with height.

270 Smoke lidar ratio is usually assumed to be higher than that of dust (Tesche et al., 2011;

271 Burton et all., 2012), meanwhile in Fig 5c the lidar ratio S$_{532}$ is not increased in presence of the

272 smoke particles. It should however be noticed that our results were obtained at low RH. The smoke

273 particles are hygroscopic and the lidar ratio should increase with RH. The way to characterize S_{532}^{s}

274 over Dakar site can be based on the analysis of the lidar measurements during smoke episodes

275 within height range where smoke contribution becomes predominant. The results of such analysis

276 will be discussed later in section 3.3.

277

278 **3.2. Dust episodes on 14 and 24 April 2015**.

279 In the second part of April 2015, dust AOD$_{532}$ exceeded 1.0 (Fig.1b) and contributions of

280 other aerosol components were insignificant. Meanwhile, as follows from Fig.2, SSA$_{440}$ increased

281 after 15 April, thus dust became less absorbing in the UV, which should influence the lidar-derived

282 aerosol intensive properties. Fig.9 shows the values of the extinction coefficients and lidar ratios

283 at 355 nm and 532 nm, together with depolarization ratio δ$_{532}$ and the Ångström exponents A_{α} and

284 A_{β} observed on 14 April (00:00 – 05:00 UTC) and 23-24 April (23:00-06:00 UTC). The first case

285 is a "transition day" when SSA$_{440}$ starts to increase. The aerosol extinction profiles presented in

286 Fig.9a show that two dust layers can be distinguished. In the first layer (below 2.5 km), aerosol

287 intensive properties are similar to that of 1-4 April with S$_{355}$>S$_{532}$, slightly negative A$_{\alpha}$ = -0.1 and

288 A_{β} as low as -0.35. In the second layer S$_{355}$ and S$_{532}$ coincide and both A_{α} and A_{β} are close to zero.

289 The depolarization ratio in the second layer is about 31%, slightly lower than in the first one. Thus,

290 we can assume that increase of the imaginary part in UV in the first layer is more significant, than

9

291   in the second one. From the analysis of airmass back-trajectories given in Fig.10, we can conclude

292   that the air masses in the first layer originate from the Northeastern/Eastern drylands, while in the

293   second layer the air masses arrive from the East. After 14 April, S_{355} and S_{532} coincided for the

294   whole height range and results obtained on 23-24 April (Fig.8 c, d) are the example of such

295   observations. Airmass back-trajectories show that the air masses at both 2.0 and 3.0 km height are

296   transported from East. The ratio S_{355}/S_{532} is close to 1.0 within the whole dust layer and both

297   Ångström exponents A_α, A_β are close to zero. Thus, the results from Figs.9, 10 are indicating that

298   lidar-derived aerosol properties depend on the dust source origin.

299

300   **3.3 Analysis of lidar ratio variations in March – April 2015**

301   Fig.11 summarizes the lidar ratio measurements for period from 29 March to 24 April 2015

302   (first phase of SHADOW ended on 25 April). Here we focus on the properties of "pure dust", thus

303   do not show results before 29 March, when AOD was lower and the contribution of other aerosol

304   types could be significant (Fig.1). For the Fig.11 we have chosen height intervals, where S value

305   is stable and δ exceeds 30%. For example, on 14 and 24 April lidar ratios are averaged inside 2.7-

306   3.7 km and 2.0-4.0 km layers respectively. For the period considered, S_{355} and S_{532} vary in the

307   ranges 50 sr – 80 sr and 45 sr - 60 sr respectively with a mean values of 62 sr and 51 sr. Enhanced

308   variability of S_{355} compared to S_{532} can be explained by variation of the imaginary part at 355 nm.

309   At the beginning of the 29 March and 8 April dust episodes, S_{355}/S_{532} ratio is as high as 1.5 and

310   then gradually decreases. After 14 April, S_{355}/S_{532} ratio becomes close to 1.0, thus S presents no

311   spectral dependence.

312   The day-to-day variation of the aerosol column properties, including the spectrally

313   dependent complex refractive index, can be obtained from AERONET (Holben et al., 1998).

314   Fig.12 shows the imaginary part of the aerosol refractive index at 440 nm and 675 nm (Im_{440},

315   Im_{675}) provided by AERONET for the same period of time as in Fig.11. The Im_{440} strongly

316   decreases after 14 April, correlating with the decrease of S_{355}/S_{532} ratio in Fig.11, which

317   corroborates the suggestion, that variations of S_{355}/S_{532} ratio are related to variation of dust

318   absorption in the UV. The retrieved real part (Re) of the complex refractive index oscillates around

319   Re=1.45 and shows no significant spectral dependence. Correlation between enhancement of

320   Im_{440}, with in respect to Im_{675}, and increase of lidar-derived S_{355}/S_{532} is clearly seen in Fig.13,

321   showing time – series of difference Im_{440}-Im_{675} and S_{355}/S_{532} ratio.

322   To analyze the variations of the observed lidar ratios and the Ångström exponents, a

323   simplified numerical simulation has been performed. For a realistic modeling of the dust lidar

324   ratio, various mixtures of different mineral components and particles shapes should be considered.

325   Sensitivity of the modeling results to the dust mixture parameters was demonstrated in study of

326   Gasteiger et al. (2011). Such detailed modeling, however, is out of the scope of the present paper.

327   Here we only intend to evaluate the main impact when the imaginary part of CRI is modified.

328   The lidar ratio depends not only on the complex refractive index but also on the dust

329   particle size distribution (PSD). The PSDs provided by AERONET on 2 and 23 April 2015 (three

330   distributions for each day) are shown in Fig.14. The PSDs are similar and the effective radii for

331   both days are about 0.75 μm, thus, difference in S observed for 2 and 23 April should be related

332   mainly to the complex refractive index. Fig.15a presents modeled S_{355} and S_{532} lidar ratios together

333   with the extinction and backscattering Ångström exponents A_α, A_β as a function of the imaginary

334   part. Computations were performed for the AERONET derived size distribution on 23 April from

335   Fig.14 using the assembly of randomly oriented spheroids (Dubovik et al., 2006) with the real part

336   Re=1.55. S_{355} and S_{532} increase with the imaginary part and the ratio S_{355}/S_{532} is about 1.1.

337   Extinction coefficient is slightly sensitive to the imaginary part, thus increase of S in Fig.15 is due

338   to decrease of backscattering coefficient with Im. The modeled A_α is about $A_\alpha=0.1$, while A_β

339   decreases with Im to $A_\beta=-0.2$. To estimate the influence of a spectrally dependent imaginary part

340     $Im(\lambda)$ on A_β, we have also performed computations assuming a fixed $Im_{532}=0.002$ and only Im_{355}

341   is free to vary. Corresponding results are shown in Fig.15a with open stars. Spectral dependence

342   of the imaginary part significantly decreases A_β: for $Im_{355}=0.005$ (Im_{355} – $Im_{532}=0.003$), A_β

343   decreases to -0.75.

344   We should recall however, that for the second half of April the observed ratio S_{355}/S_{532},

345   was about 1.0, and both extinction and backscatter Ångström exponents were close to zero. To

346   figure out the kind of PSD that would reproduce those observations, we retrieved the PSD from

347     $3\beta+2\alpha$ measurements, as described in Veselovskii et al. (2002, 2010). For that purpose, data from

348   23-24 April (Fig.9), averaged within 2-3 km layer, were inverted and corresponding PSD is shown

349   in Fig.14 with red line. Inversion was performed for the assembly of randomly oriented spheroids,

350   in assumption of spectrally independent refractive index. Due to the limited number of input data

351   (five) we are able to reproduce only the main features of the PSD. The maximum of this lidar

352   derived PSD is shifted towards larger radii, with respect to the AERONET size distribution, but at

353   the same time, retrieved PSD contains significant contribution from the fine particles. The

354   simulation results for this lidar derived PSD, are given by Fig.15b. The lidar ratios S_{355}, S_{532} for

355   all values of the imaginary part are close. The backscatter and extinction Ångström exponents are

356   close to zero, matching the observations of the second half of April 2015. Thus simulation results

357   demonstrate dependence on the PSD chosen, but in both cases these lead to the same conclusion:

358 observed low values of A_β can not be reproduced without accounting for spectral dependence of
359 the imaginary part.

360   To compare computations and observations, information upon Im_{355} and Im_{532} values is
361 needed. The recently measured refractive indices of dust, sampled at different regions of Africa,
362 are presented by Di Biagio et al. (2019). In particular, for the countries located North and East of
363 Senegal, the aerosol imaginary parts at 370, 470, 520, 660 nm are of 0.0043, 0.0033, 0.0026,
364 0.0013 for Mauritania and 0.0048, 0.0038, 0.0030, 0.0024 for Mali respectively. The highest
365 values of lidar ratios, observed in our measurements, are about 60 sr and 80 sr at 532 nm and 355
366 nm respectively. Corresponding imaginary parts of CRI from Fig.15 can be estimated as
367 Im_{532}=0.002-0.003 and Im_{355}=0.005-0.006, which agrees with results presented by Di Biagio et al.
368 (2019). Assuming Im_{355}=0.005 and Im_{532}=0.002, the modeled ratio S_{355}/S_{532} is about 1.44 and A_β
369 is about -0.75 for both AERONET and lidar derived PSDs, which again reasonably agrees with
370 observations. The modeling performed is very simplified, still it confirms that the observed values
371 of S_{355}/S_{532} ratio and A_β can be explained by the spectral dependence of the imaginary part of CRI.

372   Thus, based on our measurement results, two types of dust can be distinguished. The first
373 type has high S_{355}/S_{532} ratio (up to 1.5). Such kind of dust is characterized by an increase of the
374 imaginary part in the UV and it was observed, for example, during 29 March and 10 April episodes.
375 For the second type, the ratio $S_{355}/S_{532} \approx 1.0$, so variation of the imaginary part of the refractive
376 index between 532 and 355 nm wavelengths should be smaller than for the first type. Such dust
377 was observed in the second half of April 2015. Both types are characterized by high depolarization
378 ratio, δ_{532} values, exceeding 30%, so depolarization measurements at 532 nm are not capable to
379 discriminate between these two types of dust.

380   The difference in the observed dust properties is probably related to the mineralogical
381 characteristics in the source region. From the back-trajectories analysis presented in Figs. 4 and
382 10 one can suppose that the first type of dust was transported from the North–East, while the
383 second type from the East. In order to verify if a difference in the dust emission source region and
384 transport take place, we also analyzed the Infrared Difference Dust Index (IDDI) derived from the
385 Meteosat Second Generation (MSG) geostationary satellite imagery in the thermal infrared (TIR).
386 The IDDI is developed by Legrand et al. (1985, 2001) originally for the Meteosat First Generation
387 (MFG) and is based on impact of the airborne mineral dust on the TIR radiation emitted by the
388 terrestrial surface. The physical principle of the IDDI derivation is in thermal contrast between
389 terrestrial surface and atmosphere and the best sensitivity is found at around noon time when the
390 surface temperature is maximal (Legrand et al., 1988). The IDDI product shows that brightness
391 temperature of terrestrial surface observed by satellite can be reduced up to about 50°K in presence
392 of airborne mineral dust, while reduction by about 10°K already indicates a major dust event

393   (Legrand et al., 2001). A direct relationship between the IDDI and aerosol optical thickness in
394   solar spectrum and visibility was also found (Legrand et al., 2001). It should be mentioned here
395   that the IDDI was initially developed for MFG and the absolute consistence with the IDDI values
396   from MSG should be examined due to differences in spatial and spectral resolutions between two
397   sensors. However, the physical principles used for the IDDI determination are the same and a
398   direct application of the MFG IDDI algorithm to MSG was found as possible. Moreover, tests
399   showed that the absolute values of IDDI for a coincident overlapping period of MFG and MSG
400   are very close. Nevertheless, employment of the IDDI from MSG is indeed applicable for the
401   required in the current analysis purpose of solely dust spatial patterns detection.

402   The IDDI calculations, applied to the MSG images taken during the field campaign, clearly
403   show a major dust event in northern and central Africa. The elevated IDDI values over Senegal
404   are also visible. The IDDI images show distinguishable changes in the emission sources and
405   transport features during the different phases of the observations. For instance, Fig. 16 shows that
406   the dust emissions during the first phase of the event are originated in south Algeria, Mauritania
407   and Mali (examples of images from 29 and 30 March 2015). Weeks later, spatial patterns of the
408   elevated IDDI are shifted to south and show source regions in south of Niger (Fig.15c, d). Of
409   course, attribution of emission sources mineralogy to aerosol spectral absorption is a complex task
410   (Alfaro., et al 2004; Lafon et al., 2006; Di Biagio et al., 2017, 2019) and it is difficult to point to a
411   specific source that could clearly explain the observed in this study change in the aerosol absorbing
412   properties. However, the IDDI images clearly suggest a change in the dust transport regime that is
413   consistent with the change in the dust optical properties.

414

415   **4. Smoke episodes in December 2015 – January 2016**

416   During the SHADOW campaign, we had several strong smoke episodes in December 2015
417   – January 2016, when air mass transported the products of biomass burning from the areas of
418   intensive forest fires in equatorial region. The relative humidity in the advected smoke layers
419   varied from episode to episode, allowing evaluation of the RH influence on the smoke lidar ratios
420   S_{355}, S_{532}. We should keep in mind, however, that for different days the smoke particles could have
421   different chemical composition, so evaluated RH dependence can be considered as semi-
422   quantitative only. The spatio-temporal evolution of the particle backscattering coefficient and
423   depolarization ratio at 532 nm, during the 14-15 December 2015 smoke episode, is given in Fig.17.
424   The same figure shows also the water vapor mixing ratio, a convenient tracer to identify wet air
425   mass arrived from the equatorial region. The smoke particles are usually contained in elevated
426   layers, being mixed with dust (Veselovskii et al., 2018). The height ranges where the smoke

427   particles are predominant can be identified by low depolarization ratio and enhanced WVMR. For

428   event considered, the smoke particles are predominant above 1500 m after midnight.

429   The vertical profiles of α_{355}, α_{532}, S_{355}, S_{532}, A_α, A_β together with the water vapor mixing

430   ratio and the relative humidity, for 15 December (04:00 – 06:00 UTC), are shown in Fig.18. The

431   same figure presents decomposition of β_{532} to the dust and smoke contributions, based on

432   depolarization measurements (Tesche et al., 2011). The smoke episodes are characterized by

433   different relative humidity within the elevated layer. On 15 December, RH is about 40% in the

434   1500 – 2100 m range and the ratio $\dfrac{\beta^s_{532}}{\beta_{532}}$ is about of 0.57 at 2000 m. The lidar ratio S_{532} decreases

435   from 50 sr to 44 sr in 1000 m - 2000 m range, while S_{355} rises from 58 sr to 67 sr, thus S_{355}

436   significantly exceeds S_{532}. We should recall that lidar ratios presented in Fig.18 are attributed to

437   dust- smoke mixture. In principle, we can estimate S^s_{532} using Eq.5, because the ratio $\dfrac{\beta^s_{532}}{\beta_{532}}$ is

438   available. Corresponding S^s_{532} profile obtained for assumed $S^d_{532}=50$ sr is shown in Fig.18a (black

439   line). S^s_{532} is about 40 sr at 2000 m and it is close to measured S_{532} value. In the smoke layer, the

440   extinction Ångström exponent A_α, can exceed A_β, due to negative contribution of A^d_β. In particular,

441   on 15 December A_α is about 1.1, while A_β is close to zero.

442   To estimate the dependence of smoke lidar ratios S_{355} and S_{532} on RH, five smoke episodes

443   on 14-15, 15-16, 22-23, 24-25 December 2015 and 19-20 January 2016 were analyzed. S_{532} and

444   S_{355}, together with relative humidity and the $\dfrac{\beta^s_{532}}{\beta_{532}}$ ratio are summarized, for these episodes, in

445   Table 1. The heights chosen correspond to the values of relative humidity close to maximum. The

446   calculated values of RH are characterized by high uncertainties, because lidar and sonde

447   measurements are not collocated. Estimations of the corresponding uncertainties are also given by

448   Table 1. The lidar ratio values from Table 1 are plotted in Fig.19 as a function of RH. These plots,

449   however, should be taken with care, because, due to variation of chemical composition and the

450   aging processes, results may depend not only on RH. Moreover, the dust particles occurring in the

451   elevated layers, as discussed, can introduce an additional ambiguity in the results. Nevertheless,

452   Fig.19 demonstrates a clear increasing trend of S with RH, at both wavelengths. From this figure,

453   one can also conclude that S_{355} always exceeds S_{532} and, that S_{532} for smoke can be as small as

454   44±5 sr at low humidity. The small values of S_{532} for the "fresh smoke" (about 40 sr) were reported

455   also by Burton et al. (2012).

456   To compare our observations with the lidar ratios used in the MERRA-2 model, we have

457   also performed the simulation of $S_{532}^{OC}(RH)$ and $S_{355}^{OC}(RH)$ dependence for organic carbon (OC)

458   based on the particle parameters and hygroscopic growth factor from MERRA-2 model. In

459   MERRA-2 the organic carbon is the main component of the biomass burning products. The

460   imaginary part of the OC increases in the UV due to the presence of "brown carbon" (BrC), which

461   is a subset of organic carbon with strong absorption in the UV region (Bergstrom et al., 2007;

462   Torres et al., 2007). The majority of BrC is emitted into the atmosphere through low-temperature,

463   incomplete combustion of biomass. In the newest development of GEOS, biomass burning OC is

464   now emitted as a new BrC tracer species that uses $Im_{532}=0.009$ and $Im_{355}=0.048$ values (Hammer

465   et al. 2016). Thus, the spectral behavior of the imaginary part of organic carbon refractive index

466   depends on contribution of the BrC fraction to the primary organic carbon and on the physical-

467   chemical processes in the smoke layer during its transportation. As a result, the spectral

468   dependence of Im can present strong variations. In our study, the computations at 355 nm were

469   performed for four values of the imaginary part of dry particles $Im_{355}=0.048, 0.03, 0.02, 0.01$. At

470   532 nm two values $Im_{532}=0.005$ and 0.009 were considered. The parameters of the dry particle size

471   distribution, the real part of CRI and the hygroscopic growth factor used in computations are given

472   in Veselovskii et al. (2018). The particles are assumed to be homogeneous spheres and an increase

473   of the volume for every RH value (calculated from the growth factor) occurs due to water uptake.

474   Thus both the real and the imaginary part of CRI depend on RH.

475   The results of the simulations, shown in Fig.19, demonstrate strong dependence of the

476   organic carbon lidar ratio on the imaginary part of dry particles and on the relative humidity. For

477     $Im_{355}=0.048$, for all RH, S_{355} is above 95 sr, which strongly exceeds the observed values. For lower

478   Im_{355} the S_{355} (RH) dependence is more pronounced and for Im_{355} within the range 0.01-0.02,

479   computed S_{355} are close to observed values. Computed S_{532} values at low RH exceed the measured

480   ones, but for RH>70% agreement between measurements and GEOS assumed optical properties

481   for OC becomes reasonable.

482

483   **5. Summary and conclusion**

484   Our study shows the impact of the imaginary part variation on the lidar-derived dust

485   properties. In contrast to extinction, the backscattering coefficient, and so the lidar ratio, are

486   sensitive to the imaginary part of CRI. Hence, S_{355}/S_{532} ratio can be an indicator of the imaginary

487   refractive index enhancement in the UV. Measurements performed during the SHADOW

488   campaign, in dust conditions, show a correlation between the decrease of Im_{440}, derived from

489   AERONET observations, and the decrease of lidar-derived S_{355}/S_{532} ratio. Namely, in the second

490 half of April 2015, S_{355}/S_{532} decreased from 1.5 to 1.0, when Im_{440} decreased from 0.0045 to

491 0.0025. Our numerical simulations confirm, that observed S_{355}/S_{532} (ratio close to 1.5) and A_β

492 (value close to -0.75) can be due to spectral variation of the imaginary part, attributed to iron oxides

493 contained in dust particles. The simulations were performed for the model of randomly oriented

494 spheroids, however, we should recall, that increase of the particle lidar ratio with the imaginary

495 part should occur for any particle shape.

496   Thus, April 2015 observations suggest the presence of different dust types, characterized

497 by distinct spectral dependence of $Im(\lambda)$. The analysis of backward trajectories and IDDI derived

498 from MSG geostationary satellite confirms different air mass and dust particles transport features

499 in the beginning and at the end of April. Hence, the observed variations of S_{355}/S_{532} can be related

500 to the source region mineralogy. During April, the particle depolarization systematically exceeded

501 30%, therefore no discrimination between different types of dust was possible. Dependence of

502 S_{355}/S_{532} ratio on dust origin, in particular, could explain, why during SAMUM experiments no

503 significant spectral dependence of the lidar ratio was observed.

504   The results presented in this study demonstrate also that, for the selected temporal interval,

505 the dust lidar ratios may present significant variation with height. Dust of different size and

506 mineralogical composition can have different deposition rate, hence, complex refractive index can

507 be height-dependent. For instance, on April 1st, the S_{532} decreased with height from 60 sr to 50 sr

508 within 1000–3000 m range, while depolarization ratio exceeded 30%. The analysis of this episode

509 showed that variation of the lidar ratio is entirely attributed to variations of dust characteristics;

510 the smoke aerosol contribution was insignificant. The data also demonstrate that a seemingly

511 uniform dust layer may have quite a complex height variation. The results therefore suggest the

512 relevance of including a varying mineralogy in radiative and climatic modeling of desert dust

513 impacts. Dust mineralogy should be also taken into account, when possibility of the particle

514 microphysical parameters characterization on a base of multiwavelength lidar measurements is

515 analyzed (Perez-Ramirez et al., 2019, 2020).

516   During December – January, the dry season in western Africa, our observations allowed in

517 addition the analysis of biomass burning aerosol properties. These particles are a product of the

518 seasonal forest fires and intensive agricultural waste combustion and can contain a substantial

519 amount of organic compounds, characterized by an enhanced imaginary part in UV (so called

520 BrC). For this aerosol type, the $Im(\lambda)$ dependence should increase the lidar ratio at 355 nm and

521 influence S_{355}/S_{532}. The smoke particles can be also hydrophilic and the lidar ratio can therefore

522 exhibit a strong dependence on RH. Several strong smoke episodes were observed during the

523 SHADOW campaign. While we were able to evaluate the RH profiles, the dependence of the

524 smoke lidar ratio with RH has been estimated. The results obtained should be taken as semi-

16

525 qualitative only, due to possible variation of smoke particles composition from episode to episode
526 and due to the presence of dust particles. Nevertheless, the results clearly demonstrate an increase
527 of S_{532} from 44±5 sr to 66±7 sr and of S_{355} from 62±6 sr to 80±8 sr, when the RH increased from
528 25% to 85%.

529 We would like to conclude that the multi-wavelengths Raman and depolarization lidar
530 measurements in western Africa enabled quite unique and comprehensive profiling of dust and
531 smoke spectral absorption properties. The results demonstrated a high variability of the lidar ratio
532 and the presence of its spectral dependence. Our study is one of the first attempts to track aerosol
533 composition variability using lidar measurements and to understand the mechanism underlying the
534 observed variations. However, the results presented were obtained for a single region in western
535 Africa. It is important to repeat such studies at different locations around the world, including the
536 Middle East, Central and East Asia, Australia, and North Amerika in order to improve our
537 knowledge on real-world dust optical properties, needed in climate relevant atmospheric
538 modelling.

539

540 *Author contributions*. IV processed the data, and wrote the paper. QH and TP performed the
541 measurements. PG supervised the project and helped with paper preparation. MK developed
542 software for data analysis. YD and ML analyzed the satellite data and PC provided MERRA-2
543 simulations.
546 *Competing interests*. The authors declare that they have no conflict of interest.

556

557

558

559

560

561 Table 1. Lidar ratios S_{355}, S_{532} for five smoke episodes in December 2015 – January 2016 and
562 corresponding the relative humidity RH. The table provides also the height and temporal interval

563 of observations. The contribution of the smoke particles to the total backscattering $\frac{\beta_{532}^s}{\beta_{532}}$ is derived

564 from depolarization measurements.
565

Date	Height, m	Time, UTC	$\frac{\beta_{532}^s}{\beta_{532}}$	RH, %	S_{355}, sr	S_{532}, sr
15 Dec	2000	04:00-06:00	0.57	42±8	67±7	44±5
15 Dec	1850	19:20-20:30	0.57	25±6	62±6	50±5
23 Dec	2250	05:00-07:00	0.65	65±13	76±8	56±6
24 Dec	3200	19:00-23:00	0.66	75±14	76±8	62±6
20 Jan	4500	01:00-07:00	0.8	85±15	80±8	66±7

566
567

568 **References**

569 Amiridis, V., Balis, D. S., Kazadzis, S., Bais, A., Giannakaki, E., Papayannis, A., and Zerefos, C.:

570   Four-year aerosol observations with a Raman lidar at Thessaloniki, Greece, in the framework

571   of European Aerosol Research Lidar Network (EARLINET), J. Geophys. Res., 110, D21203,

572   doi:10.1029/2005JD006190, 2005.

573 Alfaro, S. C., Lafon, S., Rajot, J. L., Formenti, P., Gaudichet, A., and Maille, M.: Iron oxides and

574   light absorption by pure desert dust: An experimental study, J. Geophys. Res., 109, D08208,

575   doi:08210.01029/02003JD004374, 2004.

576 Ansmann, A., Wandinger, U., Riebesell, M., Weitkamp, C.and Michaelis,W., "Independent

577   measurement of extinction and backscatter profiles in cirrus clouds by using a combined Raman

578   elastic-backscatter lidar", Appl. Opt. 31, 7113–7131, 1992.

579 Ansmann, A., Petzold, A., Kandler, K., Tegen, I., Wendisch, M., Müller, D., Weinzierl, B., Müller,

580   T., Heintzenberg, J.: Saharan Mineral Dust Experiments SAMUM–1 and SAMUM–2: what

581   have we learned?, Tellus, 63B, 403–429, 2011.

582 Burton, S. P., Ferrare, R. A., Hostetler, C. A., Hair, J.W., Rogers, R. R., Obland, M. D., Butler,

583   C. F., Cook, A. L., Harper, D. B., and Froyd, K. D.: Aerosol classification using airborne

584   High Spectral Resolution Lidar measurements – methodology and examples, Atmos. Meas.

585   Tech., 5, 73–98, doi:10.5194/amt-5-73-2012, 2012.

586 Burton, S. P., Vaughan, M. A., Ferrare, R. A. and Hostetler, C. A.: Separating mixtures of aerosol

587   types in airborne High Spectral Resolution Lidar data. Atmos. Meas. Tech., 7, 419–436, 2014.

588 Di Biagio, C., Formenti, P., Balkanski, Y., Caponi, L., Cazaunau, M., Pangui, E., Journet, E.,

589   Nowak, S., Caquineau, S., Andreae, M. O., Kandler, K., Saeed, T., Piketh, S., Seibert, D.,

590   Williams, E., and Doussin, J.-F.: Global scale variability of the mineral dust long-wave

591   refractive index: a new dataset of in situ measurements for climate modeling and remote

592   sensing, Atmos. Chem. Phys., 17, 1901-1929, https://doi.org/10.5194/acp-17-1901-2017,

593   2017.

594 Di Biagio, C., Formenti, P., Balkanski, Y., Caponi, L., Cazaunau, M., Pangui, E., Journet, E.,

595   Nowak, S., Andreae, M. O., Kandler, K., Saeed, T., Piketh, S., Seibert, D., Williams, E., and

596   Doussin, J. – F.: Complex refractive indices and single scattering albedo of global dust aerosols

597   in the shortwave spectrum and relationship to iron content and size, Atm. Chem. Phys., 19,

598   15503–15531, 2019.

599 Dubovik, O., Sinyuk, A., Lapyonok, T., Holben, B.N., Mishchenko, M., Yang, P., Eck, T.F.,

600   Volten, H., Munoz, O., Veihelmann, B., van der Zande, W.J., Leon, J.-F., Sorokin, M.,

601   Slutsker, I.: Application of spheroid models to account for aerosol particle nonsphericity in

602   remote sensing of desert dust, *J. Geophys. Res*., 111, D11208, doi:10.1029/2005JD006619,
603   2006.

604 Esselborn, M., Wirth, M., Fix, A., Weinzierl, B., Rasp, K., Tesche, M., and Petzold, A.: Spatial
605   distribution and optical properties of Saharan dust observed by airborne high spectral resolution
606   lidar during SAMUM 2006, Tellus B, 61, 131–143, doi:10.1111/j.1600-0889.2008.00394.x,
607   2009.

608 Freudenthaler,V., Esselborn, M.,Wiegner, M.,Heese, B., Tesche, M. and co-authors:
609   Depolarization ratio profiling at severalwavelengths in pure Saharan dust during SAMUM
610   2006, *Tellus* 61B, 165–179, 2009.

611 Gasteiger, J., Wiegner, M., Groß, S., Freudenthaler, V., Toledano, C., Tesche, M., and Kandler,
612   K.: Modeling lidar-relevant optical properties of complex mineral dust aerosols, Tellus B,
613   63, 725-741, 2011.

614 Gelaro, R., McCarty, W., Suarez, M.J., Todling, R., Molod, A., Takacs, L., Randles, C.A.,
615   Darmenov, A., Bosilovich, M.G., Reichle, R., Wargan, K., Coy, L., Cullather, R., Draper,
616   C., Akella, S., Buchard, V., Conaty, A., Da Silva, A.M., Gu, W., Kim, G.K., Koster, R.,
617   Lucchesi, R., Merkova, D., Nielsen, J.E., Partyka, G., Pawson, S., Putman, W., Rienecker,
618   M., Schubert, S.D., Sienkiewicz, M., and Zhao, B.: The Modern-Era Retrospective Analysis
619   for Research and Applications, Version 2 (MERRA-2), Journal of Climate, 30, 5419-5454
620   2017.

621 Giannakaki, E., van Zyl, P. G., Müller, D., Balis, D., and Komppula, M.: Optical and
622   microphysical characterization of aerosol layers over South Africa by means of multi-
623   wavelength depolarization and Raman lidar measurements, Atmos. Chem. Phys., 16, 8109–
624   8123, 2016.

625 Groß, S., Tesche, M., Freudenthaler, V., Toledano, C., Wiegner, M., Ansmann, A., Althausen, D.,
626   and Seefeldner, M.: Characterization of Saharan dust, marine aerosols and mixtures of
627   biomassburning aerosols and dust by means of multi-wavelength depolarization and Raman
628   lidar measurements during SAMUM 2, Tellus B, 63, 706724, doi:10.1111/j.1600-
629   0889.2011.00556.x, 2011.

630 Groß, S., Freudenthaler, V., Schepanski, K., Toledano, C., Schäfler, A., Ansmann, A., and
631   Weinzierl, B.: Optical properties of long-range transported Saharan dust over Barbados as
632   measured by dual-wavelength depolarization Raman lidar measurements, Atmos. Chem.
633   Phys., 15, 11067–11080, https://doi.org/10.5194/acp-15-11067-2015, 2015.

634 Haarig, M., Ansmann, A., Althausen, D., Klepel, A., Groß, S., Freudenthaler, V., Toledano, C.,
635   Mamouri, R.-E., Farrell, D. A., Prescod, D. A., Marinou, E., Burton, S. P., Gasteiger, J.,
636   Engelmann, R., and Baars, H.: Triple-wavelength depolarization ratio profiling of Saharan dust

over Barbados during SALTRACE in 2013 and 2014, Atmos. Chem. Phys., 17, 10767–10794, 2017.

Haywood, J. M., Pelon, J., Formenti, P., Bharmal, N., Brooks, M., Capes, G., Chazette, P., Chou, C., Christopher, S., Coe, H., Cuesta, J., Derimian, Y., Desboeufs, K., Greed, G., Harrison, M., Heese, B., Highwood, E. J., Johnson, B., Mallet, M., Marticorena, B., Marsham, J., Milton, S., Myhre, G., Osborne, S. R., Parker, D. J., Rajot, J. L., Schulz, M., Slingo, A., Tanre, D., and Tulet, P.: Overview of the Dust and Biomass-burning Experiment and African Monsoon Multidisciplinary Analysis Special Observing Period-0, Journal of Geophysical Research-Atmospheres, 113, 10.1029/2008jd010077, 2008.

Hammer, M. S., Martin, R. V., van Donkelaar, A., Buchard, V., Torres, O., Ridley, D. A., and Spurr, R. J. D.: Interpreting the ultraviolet aerosol index observed with the OMI satellite instrument to understand absorption by organic aerosols: implications for atmospheric oxidation and direct radiative effects, Atmos. Chem. Phys., 16, 2507–2523, 2016.

Hess, M., Koepke, P., and Schult, I.: Optical properties of aerosols and clouds: The software package OPAC, Bulletin of the American Meteorological Society, 79, 831–844, 1998.

Hofer, J., Althausen, D, Abdullaev, S. F., Makhmudov, A. N., Nazarov, B. I., Schettler, G., Engelmann, R., Baars, H., Fomba, K. W., Müller, K., Heinold, B., Kandler, K., and Ansmann, A.: Long-term profiling of mineral dust and pollution aerosol with multiwavelength polarization Raman lidar at the Central Asian site of Dushanbe, Tajikistan: case studies, Atmos. Chem. Phys., 17, 14559–14577, 2017.

Hofer, J., Ansmann, A., Althausen, D., Engelmann, R., Baars, H., Abdullaev, S.F., and Makhmudov, A.N.: Long-term profiling of aerosol light-extinction, particle mass, cloud condensation nuclei, and ice-nucleating particle concentration over Dushanbe, Tajikistan, in Central Asia, Atm. Chem. Phys. Disc. doi.org/10.5194/acp-2019-963.

Holben, B.N., Eck, T.F., Slutsker, I., Tanre, D., Buis, J.P., Setzer, A., Vermote, E., Reagan, J.A., Kaufman, Y.J., Nakajima, T., Lavenu, F., Jankowiak, I., Smirnov, A.: AERONET- A federated instrument network and data archive for aerosol characterization. Remote Sensing of Environment 66, 1-16, 1998.

IPCC: Climate Change 2013: The Physical Science Basis. Contribution of Working Group I to the Fifth Assessment Report of the Intergovernmental Panel on Climate Change, edited by: Stocker, T. F., Qin, D., Plattner, G.-K., Tignor, M., Allen, S. K., Boschung, J., Nauels, A., Xia, Y., Bex, V., and Midgley, P. M., Cambridge University Press, Cambridge, UK and New York, NY, USA, 1535 pp., https://doi.org/10.1017/CBO9781107415324, 2013.

Kandler, K., Lieke, K., Benker, N., Emmel, C., Küpper, M., Müller-Ebert,D., Ebert, M., Scheuvens, D., Schladitz, A., Schütz, L., Weinbruch, S.: Electron microscopy of particles

collected at Praia, Cape Verde, during the Saharan Mineral Dust Experiment: Particle chemistry, shape, mixing state and complex refractive index. Tellus 63B, 475-496, 2011.

Kirchstetter, T. W., Novakov, T., and Hobbs, P. V.: Evidence that the spectral dependence of light absorption by aerosols is affected by organic carbon, J. Geophys. Res.-Atmos., 109, D21208, https://doi.org/10.1029/2004JD004999, 2004.

Klett J.D., "Lidar inversion with variable backscatter/extinction ratios", Appl.Opt. 24, 1638-1643, 1985.

Lafon, S., Sokolik, I. N., Rajot, J. L., Caquineau, S., & Gaudichet, A.: Characterization of iron oxides in mineral dust aerosols: Implications for light absorption. Journal of Geophysical Research, 111(D21), 2006. https://doi.org/10.1029/2005JD007016

Legrand, M., Bertrand, J. J., Desbois, M., Menenger, L., and Fouquart, Y.: The potential of infrared sattelite data for the retrieval of Saharan – dust optical depth over Africa, Journal of Applied Meteorology, 28, 309-319, 1989.

Legrand, M., Plana-Fattori, A., and N'Doume, C.: Satellite detection of dust using the IR imagery of Meteosat 1. Infrared difference dust index, Journal of Geophysical Research-Atmospheres, 106, 18251-18274, 2001.

Mamouri, R. E., Ansmann, A., Nisantzi, A., Kokkalis, P., Schwarz, A., and Hadjimitsis, D.: Low Arabian dust extinction-to- backscatter ratio, Geophys. Res. Lett., 40, 4762–4766, 2013.

Mattis, I., Ansmann, A., Müller, D., Wandinger, U., and Althausen, D.: Dual-wavelength Raman lidar observations of the extinction-to-backscatter ratio of Saharan dust, Geophys. Res. Lett., 29, 1306, doi:10.1029/2002GL014721, 2002.

Meng, Z., Yang, P., Kattawar, G. W., Bi, L., Liou, K. N., Laszlo, I.: Single-scattering properties of tri-axial ellipsoidal mineral dust aerosols: A database for application to radiative transfer calculations, J. Aerosol Science 41, 501–512, 2010.

Mona, L., Amodeo, A., Pandolfi, M., and Pappalardo, G.: Saharan dust intrusions in the Mediterranean area: three years of Raman lidar measurements, J. Geophys. Res., 111, D16203, doi:10.1029/2005JD006569, 2006.

Nicolae D., A. Nemuc, D. Müller, C. Talianu, J. Vasilescu, L. Belegante, and A. Kolgotin: Characterization of fresh and aged biomass burning events using multi-wavelength Raman lidar and mass spectrometry, J. Geophys. Res. 118, 2956–2965, doi:10.1002/jgrd.50324, 2013.

Nisantzi, A., Mamouri, R. E., Ansmann, A., Schuster, G. L., and Hadjimitsis, D. G.: Middle East versus Saharan dust extinction-to-backscatter ratios, Atmos. Chem. Phys., 15, 7071–7084, 2015.

706 Papayannis, A., Amiridis, V., Mona, L., Tsaknakis, G., Balis, D., Bösenberg, J., Chaikovski, A.,
707   De Tomasi, F., Grigorov, I., Mattis, I., Mitev, V., Müller, D., Nickovic, S., Pérez, C.,
708   Pietruczuk, A., Pisani, G., Ravetta, F., Rizi, V., Sicard, M., Trickl, T., Wiegner, M., Gerding,
709   M., Mamouri, R. E., D'Amico, G., and Pappalardo, G.: Systematic lidar observations of
710   Saharan dust over Europe in the frame of EARLINET (2000–2002), J. Geophys. Res., 113,
711   D10204, doi:10.1029/2007JD009028, 2008.

712 Papayannis, A., Mamouri, R. E., Amiridis, V., Remoundaki, E., Tsaknakis, G., Kokkalis, P.,
713   Veselovskii, I., Kolgotin A., Nenes, A. and Fountoukis, C.: Optical-microphysical properties of
714   Saharan dust aerosols and composition relationship using a multi-wavelength Raman lidar, in
715   situ sensors and modelling: a case study analysis", Atmos. Chem. Phys. 12, 4011-4032 (2012).

716 Perez-Ramirez, D., Whiteman D.N., Veselovskii, I., Colarco, P., Korenski, M., da Silva, A.:
717   Retrievals of aerosol single scattering albedo by multiwavelength lidar measurements:
718   Evaluations with NASA Langley HSRL-2 during discover-AQ field campaigns, *Remote*
719   *Sensing of Environment*, 222, 144-164, 2019.

720 Perez-Ramirez, D., Whiteman, D.N., Veselovskii, I., Korenski, M., Colarco, P., and da Silva, A.:
721   Optimized profile retrievals of aerosol microphysical properties from simulated spaceborne
722   multiwavelength lidar, Journal of Quantitative Spectroscopy & Radiative Transfer, 246,
723   106932, 2020. https://doi.org/10.1016/j.jqsrt.2020.106932

724 Perrone, M. R., Barnaba, F., De Tomasi, F., Gobbi, G. P., and Tafuro, A. M.: Imaginary refractive-
725   index effects on desert-aerosol extinction versus backscatter relationships at 351 nm: numerical
726   computations and comparison with Raman lidar measurements, Appl. Opt., 43, 5531 – 5541,
727   2004.

728 Preißler, J., Wagner, F., Guerrero-Rascado, J. L., and Silva, A. M.: Two years of free-tropospheric
729   aerosol layers observed over Portugal by lidar, J. Geophys. Res.-Atmos., 118, 3676–3686,
730   doi:10.1002/jgrd.50350, 2013.

731 Randles, C.A., Da Silva, A.M., Buchard, V., Colarco, P.R., Darmenov, A., Govindaraju, R.,
732   Smirnov, A., Holben, B., Ferrare, R., Hair, J., Shinozuka, Y., and Flynn, J.: The MERRA-2
733   Aerosol Reanalysis, 1980 Onward. Part I: System Description and Data Assimilation
734   Evaluation, J. of Climate, 30, 6823-6850, 2017.

735 Rittmeister, F., Ansmann, A., Engelmann, R., Skupin, A., Baars, H., Kanitz, T., and Kinne, S.:
736   Profiling of Saharan dust from the Caribbean to western Africa – Part 1: Layering structures
737   and optical properties from shipborne polarization/Raman lidar observations, Atmos. Chem.
738   Phys., 17, 12963–12983, https://doi.org/10.5194/acp-17-12963-2017, 2017.

739 Sakai, T., Nagai, T., Nakazato, M., Mano, Y., and Matsumura, T.: Ice clouds and Asian dust
740   studied with lidar measurements of particle extinction-to-backscatter ratio, particle

741   depolarization, and water-vapor mixing ratio over Tsukuba, Appl. Optics, 42, 7103–7116,
742   2003.

743   Shin, S.-K., Tesche, M., Kim, K., Kezoudi, M., Tatarov, B., Müller. D., and Noh, Y.: On the
744   spectral depolarization and lidar ratio of mineral dust provided in the AERONET version 3
745   inversion product, Atm. Chem. Phys., 18, 12735–12746, 2018.

746   Sokolik, I. N., and Toon, O.B.: Incorporation of mineralogical composition into models of the
747   radiative properties of mineral aerosol from UV to IR wavelengths, J. Geophys. Res. 104, D8,
748   9423 – 9444, 1999.

749   Soupiona, O., Papayannis, A., Kokkalis, P., Mylonaki, M., Tsaknakis, G., Argyrouli, A., and
750   Vratolis, S.: Long-term systematic profiling of dust aerosol optical properties using the
751   EOLE NTUA lidar system over Athens, Greece (2000-2016), *Atmospheric Environment*,
752   **183**, 165-184, 2018.

753   Soupiona, O., Samaras, S., Ortiz-Amezcua, P., Böckmann, C., Papayannis, A., Moreira, G. A.,
754   Benavent-Oltra, J. A., Guerrero-Rascado, J. L., Bedoya-Velásquez, A. E., Olmo, F. J.,
755   Román, R., Kokkalis, P., Mylonaki, M., Alados-Arboledas, L., Papanikolaou, C. A.,
756   Foskinis, R.: Retrieval of optical and microphysical properties of transported Saharan dust
757   over Athens and Granada based on multi-wavelength Raman lidar measurements: Study of
758   the mixing processes, *Atmospheric Environment*, 214,
759   doi.org/10.1016/j.atmosenv.2019.116824, 116824, 2019

760   Sun, H., Biedermann, L., and Bond, T. C.: Color of brown carbon: A model for ultraviolet and
761   visible light absorption by organic carbon aerosol, Geophys. Res. Lett., 34, L17813,
762   https://doi.org/10.1029/2007GL029797, 2007.

763   Tesche, M., Ansmann, A., Müller, D., Althausen, D., Mattis, I., Heese, B., Freudenthaler, V.,
764   Wiegner, M., Eseelborn, M., Pisani, G., and Knippertz, P.: Vertical profiling of Saharan dust
765   with Raman lidars and airborne HSRL in southern Morocco during SAMUM, Tellus B, 61,
766   144–164, 2009.

767   Tesche, M., Groß, S., Ansmann, A., Müller, D., Althausen, D., Freudenthaler, V., and Esselborn,
768   M.: Profiling of Saharan dust and biomass-burning smoke with multiwavelength polarization
769   Raman lidar at Cape Verde, Tellus B, 63, 649–676, doi:10.1111/j.1600-0889.2011.00548.x,
770   2011.

771   Torres, O., Tanskanen, A., Veihelmann, B., Ahn, C., Braak, R., Bhartia, P.K., Veefkind, P., and
772   Levelt, P.: Aerosols and surface UV products from Ozone Monitoring Instrument
773   observations: An overview, J. Geophys. Res., 112, D24S47, doi:10.1029/2007JD008809,
774   2007.

775   Veselovskii I., Kolgotin, A., Griaznov, V., Müller, D., Wandinger, U., Whiteman, D.: Inversion
776   with regularization for the retrieval of tropospheric aerosol parameters from multi-wavelength
777   lidar sounding, Appl.Opt. 41, 3685-3699, 2002.

778   Veselovskii I., O. Dubovik, A. Kolgotin, T. Lapyonok, P. Di Girolamo, D. Summa, D. N.
779   Whiteman, M. Mishchenko, and D. Tanré, 2010: Application Of Randomly Oriented
780   Spheroids For Retrieval Of Dust Particle Parameters From Multiwavelength Lidar
781   Measurements, J. Geophys. Res., **115**, D21203, doi:10.1029/2010JD014139, 2010.

782   Veselovskii, I., Whiteman, D. N., Korenskiy, M., Suvorina, A., Perez-Ramirez, D.: Use of
783   rotational Raman measurements in multiwavelength aerosol lidar for evaluation of particle
784   backscattering and extinction, Atmos. Meas. Tech., 8, 4111–4122, 2015.

785   Veselovskii, I., Goloub, P., Podvin, T., Bovchaliuk, V., Derimian, Y., Augustin, P., Fourmentin,
786   M., Tanre, D., Korenskiy, M., Whiteman, D., Diallo, A., Ndiaye, T., Kolgotin, A., Dubovik,
787   O.: Study of African dust with multi-wavelength Raman lidar during the "SHADOW"
788   campaign in Senegal, Atm. Chem. Phys. 16, 7013–7028, 2016.

789   Veselovskii, I., P. Goloub, T. Podvin, et al.: Characterization of smoke/dust episode over West
790   Africa: comparison of MERRA-2 modeling with multiwavelength Mie-Raman lidar
791   observations, Atm. Meas. Tech. 11, 949–969, 2018.

792   Wagner, R., Ajtai, T., Kandler, K., Lieke, K., Linke, C., Müller, T., Schnaiter, M., and Vragel, M.:
793   Complex refractive indices of Saharan dust samples at visible and near UV wavelengths: a
794   laboratory study, Atmos. Chem. Phys., 12, 2491–2512, 2012.

795   Whiteman, D., Melfi, S., Ferrare, R.: Raman lidar system for measurement of water vapor and
796   aerosols in the Earth's atmosphere", Appl. Opt. 31, 3068-3082, 1992.

797   Xie, C., Nishizawa, T., Sugimoto, N., Matsui, I., and Wang, Z.: Characteristics of aerosol optical
798   properties in pollution and Asian dust episodes over Beijing, China, Appl. Opt., 47, 4945 – 4951,
799   2008.

800

801

802

803
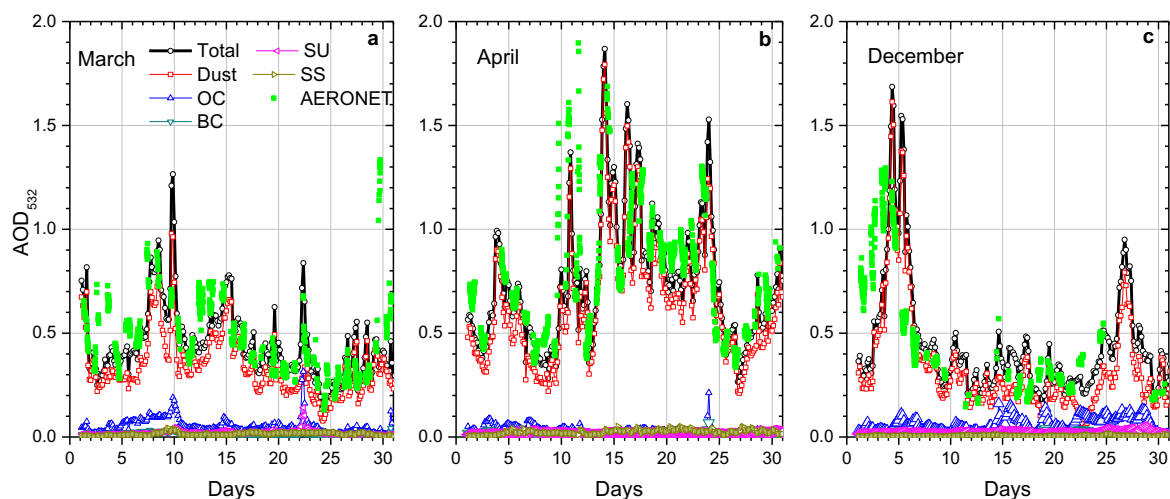
Fig.1. The aerosol optical depth (AOD) at 532 nm (open circles) and AODs of the main aerosol components, such as dust, organic carbon (OC), black carbon (BC), sulfates (SU) and sea salt (SS) provided by the MERRA-2 for (a) March, (b) April and (c) December 2015 over Mbour. Open stars show AOD$_{532}$ provided by AERONET.

808
809
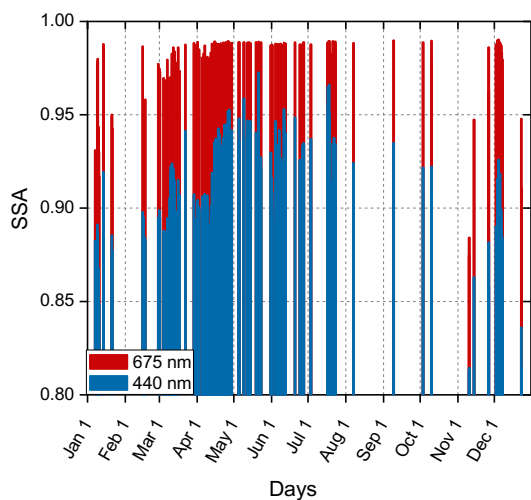
810
811   Fig.2. Aerosol single scattering albedo (SSA) at 675 nm and 440 nm provided by AERONET for
812   M'bour site in 2015.

813

26

814
815
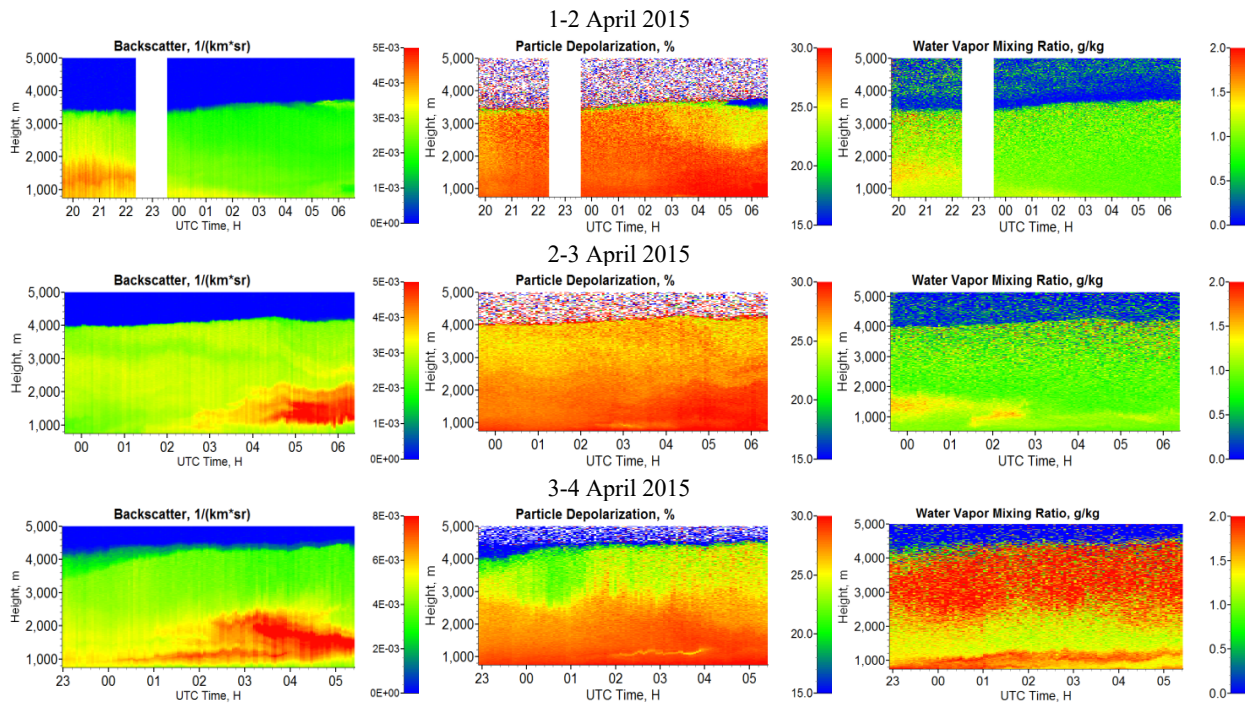
Fig.3. Tempo-spatial distributions of aerosol backscattering coefficient β_{532} (left column), particle depolarization ratio δ_{532} (middle column) and water vapor mixing ratio (right column) for the nights 1-2 April (upper row), 2-3 April (middle row) and 3-4 April 2015 (bottom row).

819

820

821

822

823
824

02 April 03:00   03 April 03:00   04 April 03:00
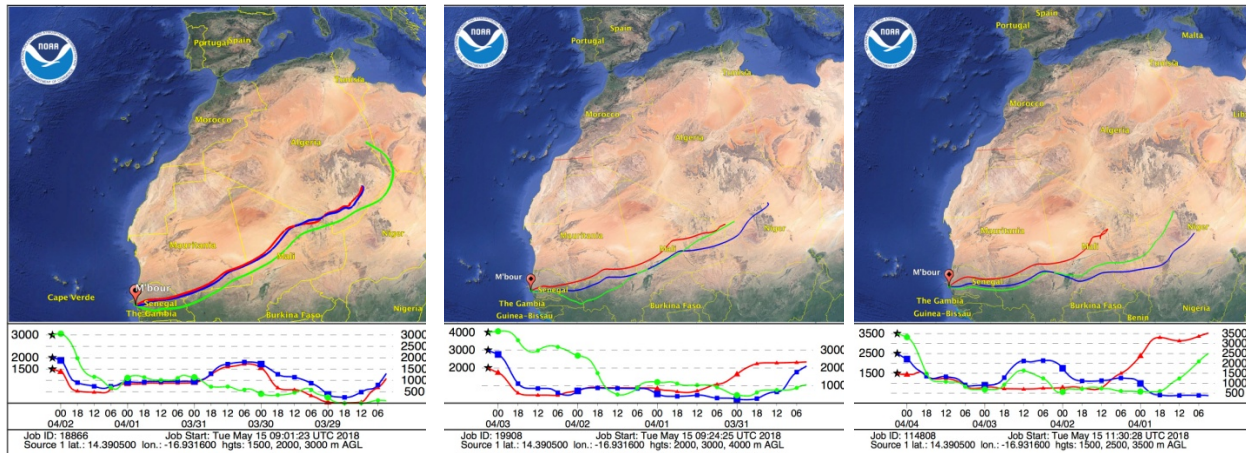
825 Fig.4. Three-day backward trajectories for the air mass in M'bour on 2, 3, 4 April 2015 at 03:00
826 UTC obtained with the HYSPLIT model.
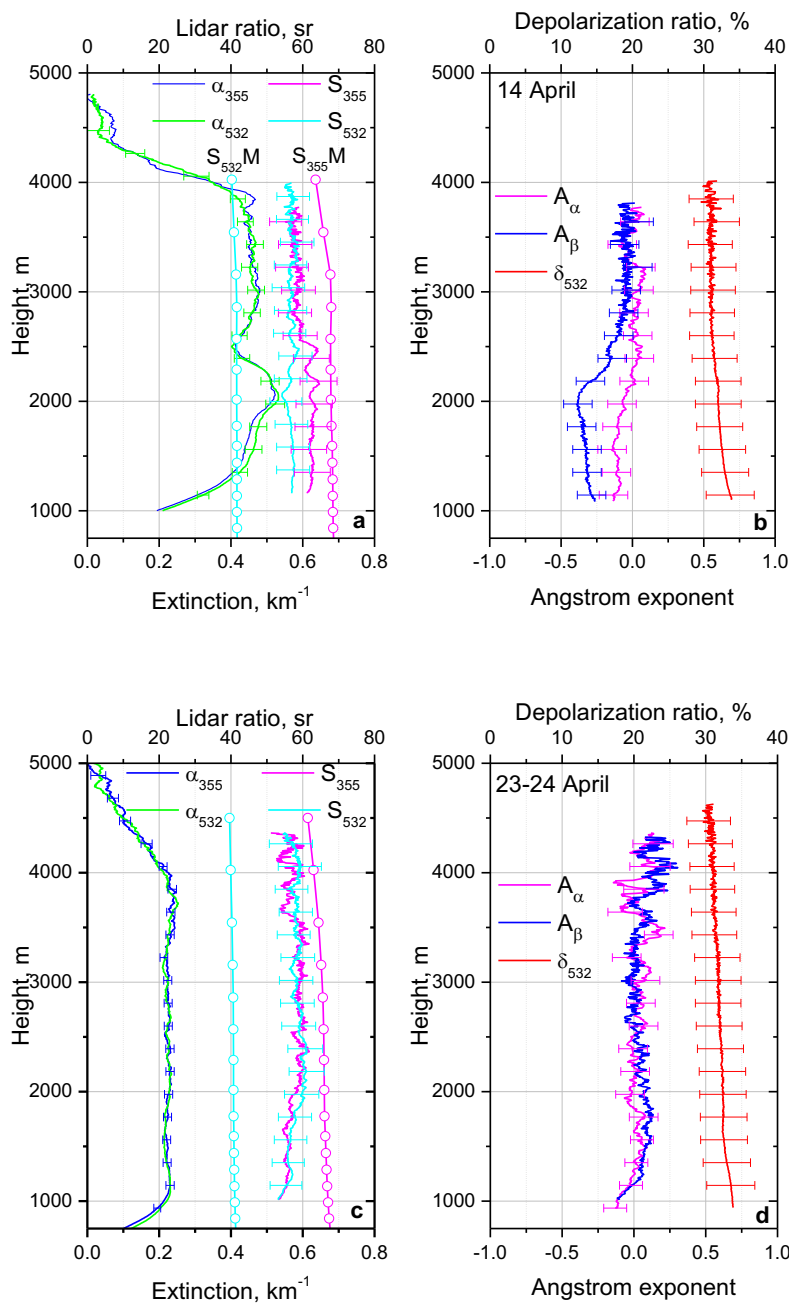827
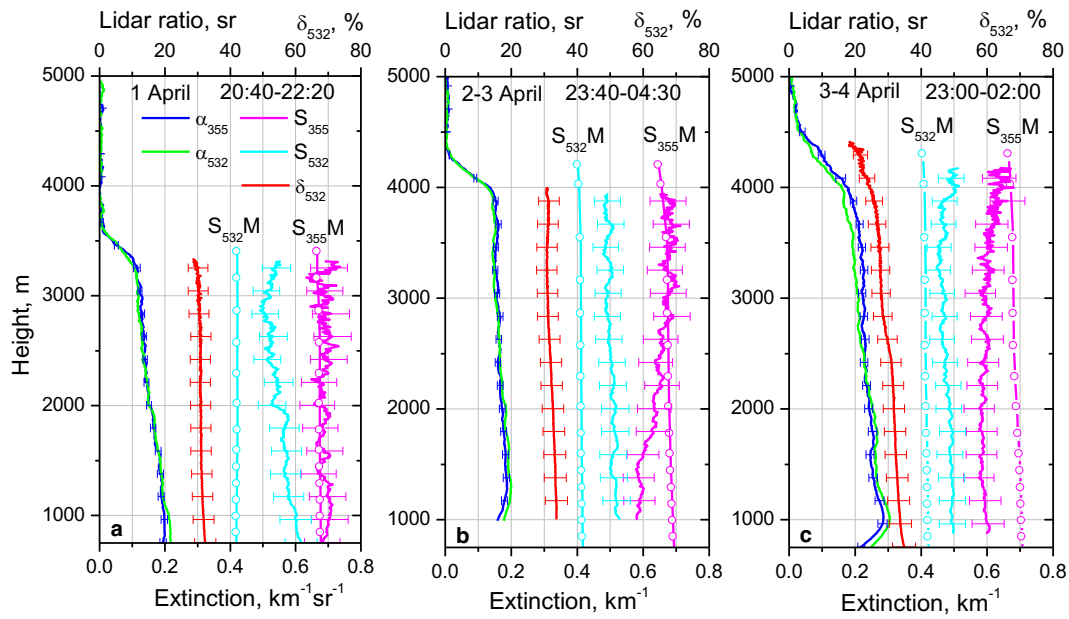
828   Fig.5. Vertical profiles of extinction coefficients (α_{355}, α_{532}) and lidar ratios (S_{355}, S_{532}) at 355 nm
829   and 532 nm together with particle depolarization ratio δ_{532} measured on 1 April (20:40-22:20
830   UTC), 2-3 April (23:40-04:30 UTC) and 3-4 April 2015 (23:00-02:00 UTC). Symbols show the
831   lidar ratios of dust provided by MERRA-2 model ($S_{355}M$, $S_{532}M$).

832
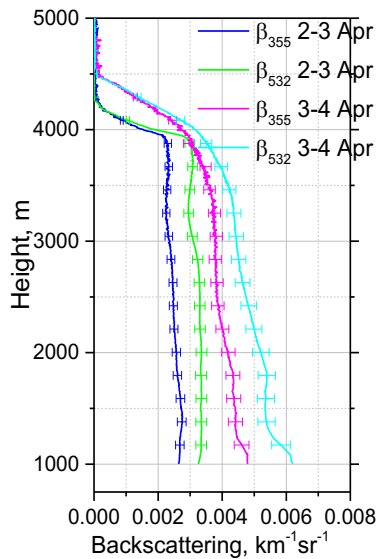
833

834   Fig.6. Backscattering coefficients for observations presented in Fig.5b,c for 2-3 and 3-4 April.

835

836

837

29

838
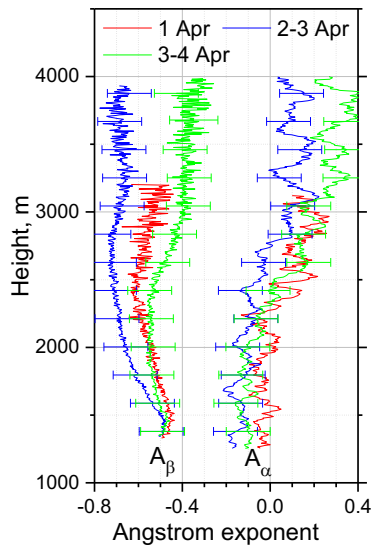
Fig.7. Vertical profiles of the extinction and backscattering Ångström exponents (A_α and A_β) at 355 – 532 nm for three temporal intervals from Fig.5.

841

842

843

844
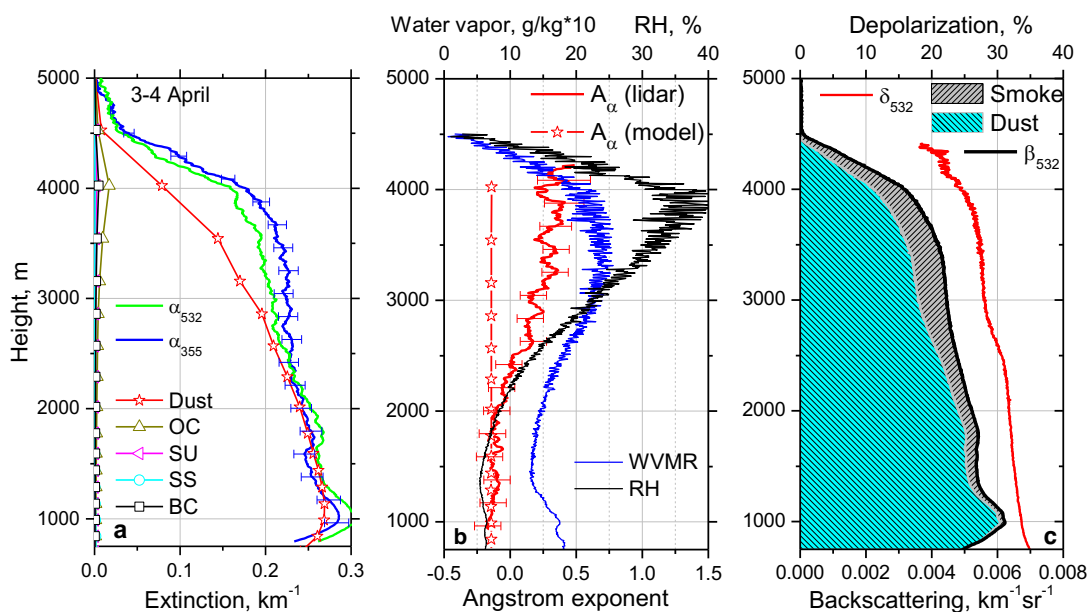
845 Fig.8. Vertical profiles of (a) extinction coefficients at 355 nm and 532 nm (α_{355}, α_{532}) measured
846 by lidar (lines) and modeled by MERRA-2 (line+symbol) for five aerosol components at 532 nm;
847 (b) extinction Ångström exponents at 355-532 nm obtained from lidar observations and modeled
848 by MERRA-2 for pure dust (stars) together with water vapor mixing ratio (WVMR) and the
849 relative humidity; (c) contribution of dust and smoke particles to β_{532} together with particle
850 depolarization ratio δ_{532}. Values of WVMR are multiplied by factor 10. Lidar measurements were
851 performed on 3-4 April 2015 for period 23:00 – 02:00 UTC. Modeling results are given for 4 April
852 00:00 UTC.

853

854

Fig.9. (a, c) Vertical profiles of extinction coefficients (α_{355}, α_{532}) and lidar ratios (S_{355}, S_{532}) at 355 nm and 532 nm; together with (b, d) particle depolarization ratio δ_{532}, and extinction and backscattering Ångström exponents (A_α, A_β) measured on (a, b) 14 April 2015 (00:00 – 05:00 UTC) and (c, d) the night 23-24 April (23:00-06:00 UTC). Open symbols on plots (a, c) show the lidar ratios $S_{355}M$ and $S_{532}M$ provided by MERRA-2 model on 14 and 14 April at 00:00 UTC.

867

868

14 April	24 April

869
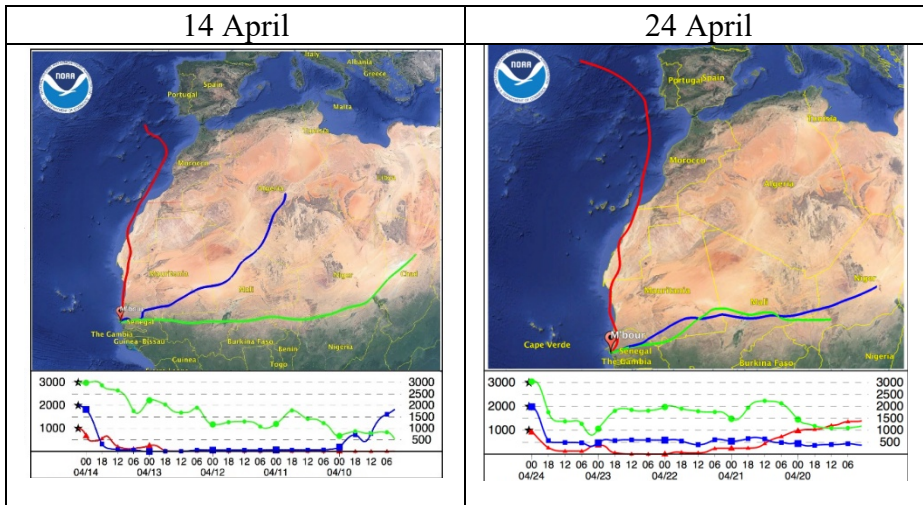
Fig.10. Four-days backward trajectories for 14 April (03:00 UTC) and 24 April (00:00 UTC)
2015 obtained with the HYSPLIT model.

872

873

874
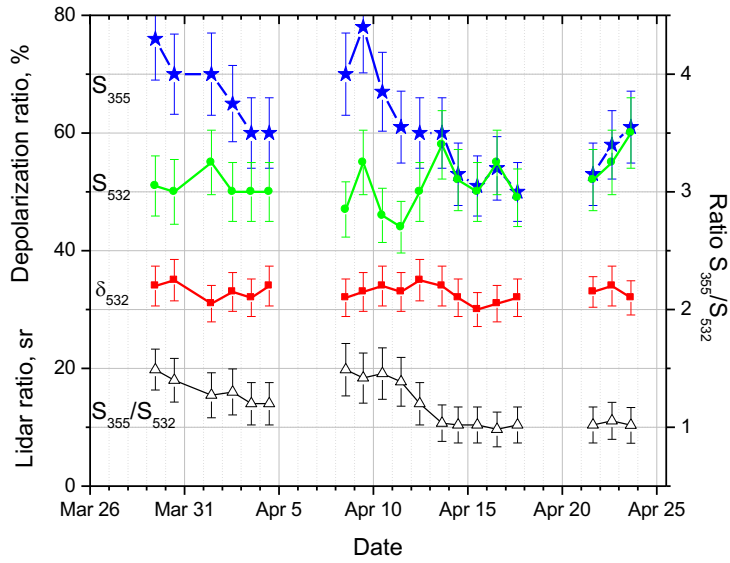
875
876 Fig.11. Lidar ratios S_{355}, S_{532} and the particle depolarization ratio δ_{532} for dust episodes in March
877 - April 2015. Open triangles show the ratio S_{355}/S_{532}.
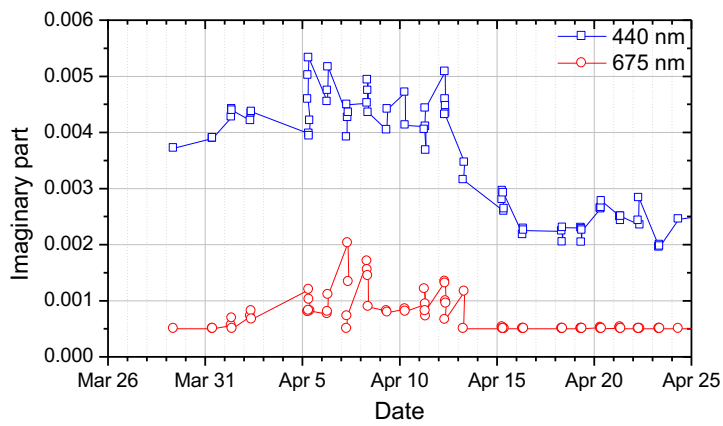
878
879 Fig.12. Imaginary part of the refractive index at 440 nm and 675 nm provided by AERONET in
880 March – April 2015
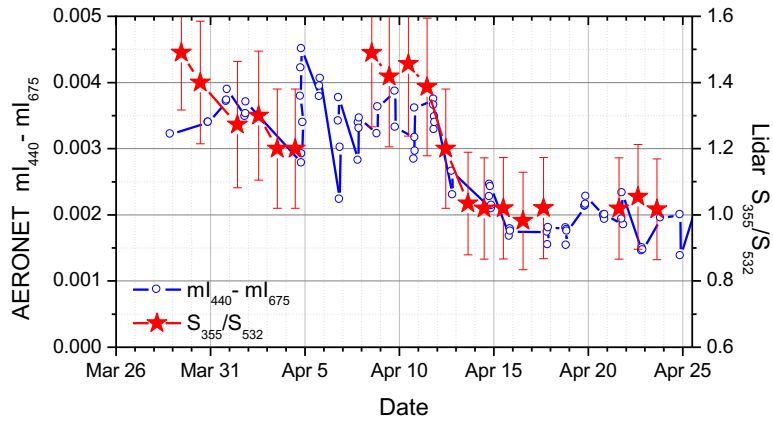
883
884   Fig.13. Difference Im_{440} - Im_{675} from Fig.11 together with lidar measured values S_{355}/S_{532} from
885   Fig.11 for days in April 2015.
886

887
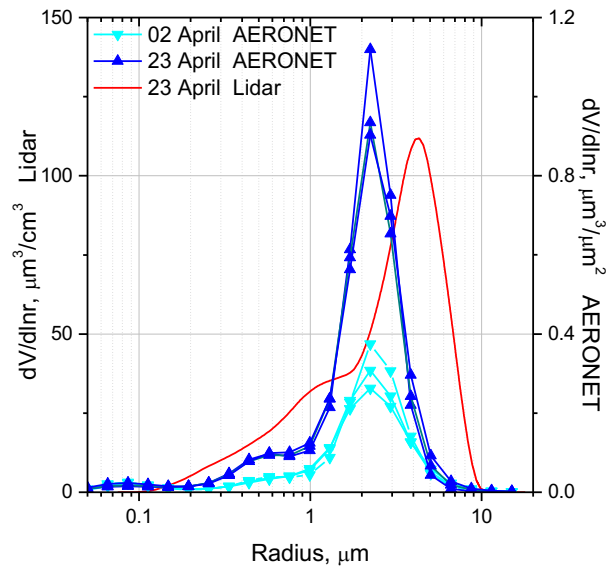
888
889 Fig.14. The particle size distributions provided by AERONET on 2 and 23 April 2015 (three PSDs
890 for each day). Red line shows the PSD derived from 3β+2α lidar measurements on 23-24 April
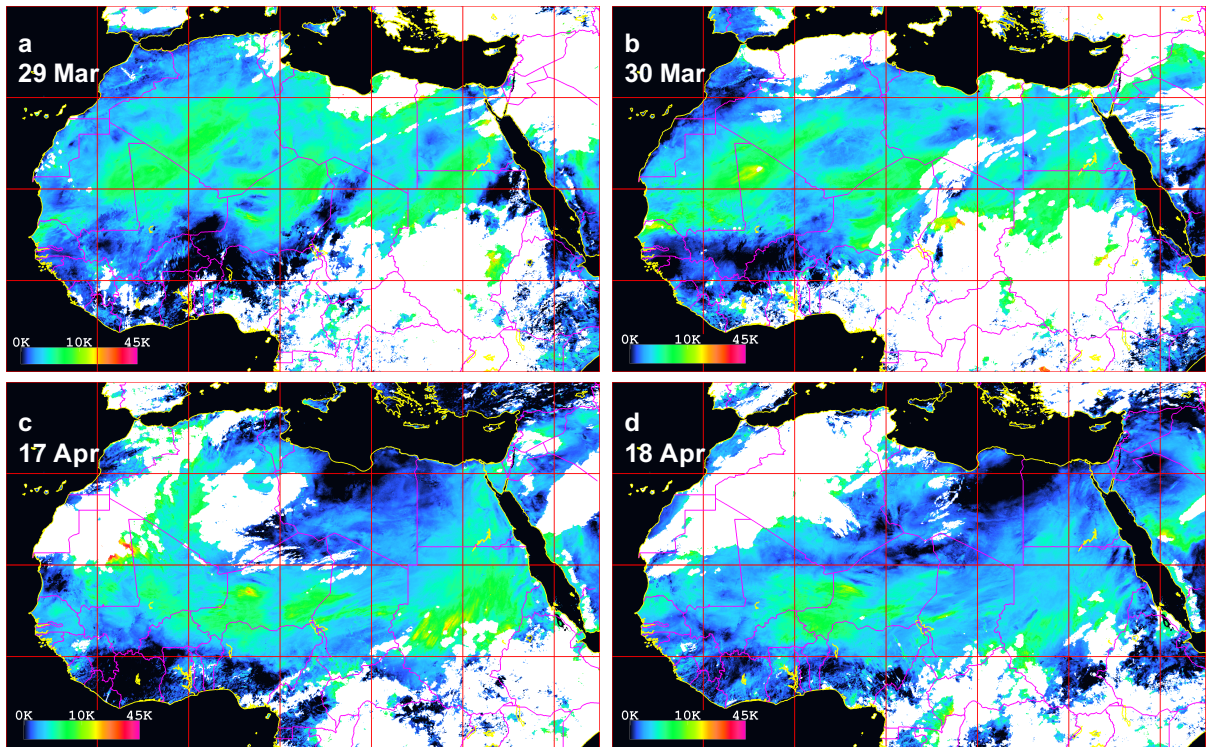891 within 2.0 – 3.0 km height range.
892
893

894
895

896
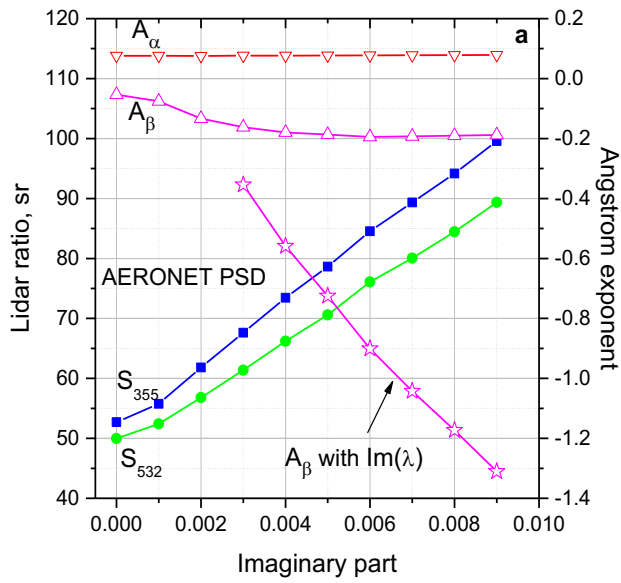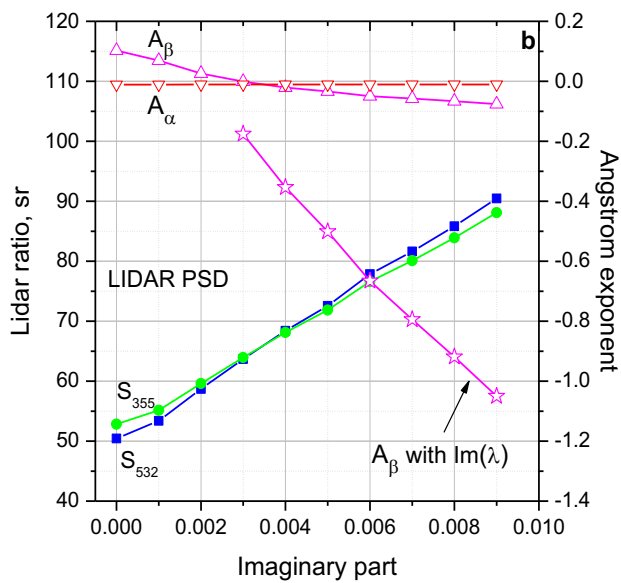
897
898
899 Fig.15. Lidar ratios S_{355}, S_{532} together with the extinction and backscattering Ångström exponents
900 A_α and A_β calculated for (a) AERONET PSD on 23 April from Fig.14 and (b) lidar derived PSD
901 from Fig.13 as a function of the imaginary part. Open stars show A_β for spectrally dependent
902 imaginary part $Im(\lambda)$, assuming that $Im_{532}=0.002$ is fixed and only Im_{355} is free vary. Computations
903 are performed for the assembly of randomly oriented spheroids with the real part Re=1.55.
904

Fig.16. Infrared Difference Dust Index (IDDI) derived from MSG geostationary satellite at noon time. Panels (a), (b) show IDDI elevated values, representing airborne dust emission and transport, over central and northern Sahara on 29, 30 March 2015. The dust transport regime is visibly changed a few days later (17, 18 April 2015, panels (c), (d)); the elevated IDDI values are shifted to the south. The areas in white are cloud screened pixels; the IDDI is derived only over land due to the algorithm physical principle.

915
916
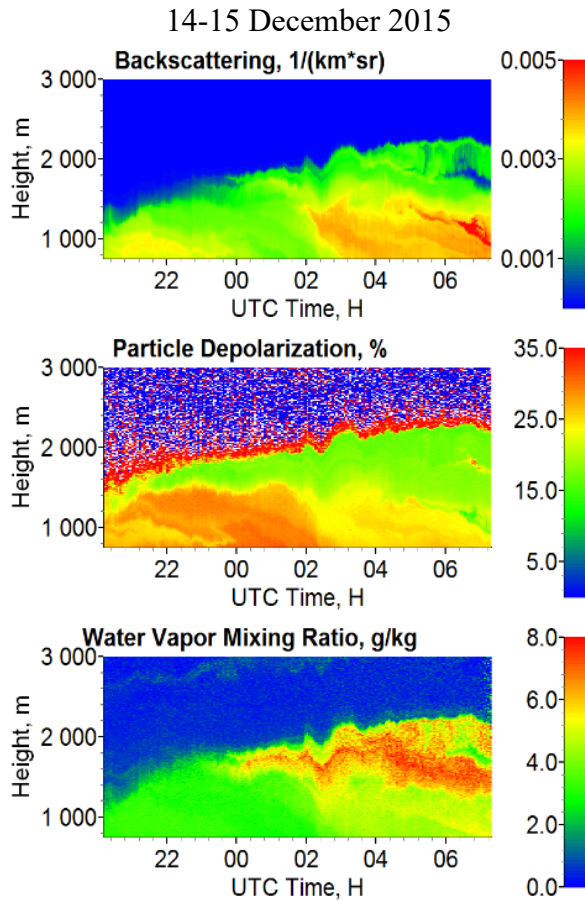
14-15 December 2015

917 Fig.17. Tempo-spatial distributions of aerosol backscattering coefficient β_{532}, particle
918 depolarization ratio δ_{532} and water vapor mixing ratio during smoke episode on the night 14-15
919 December 2015.
920
921
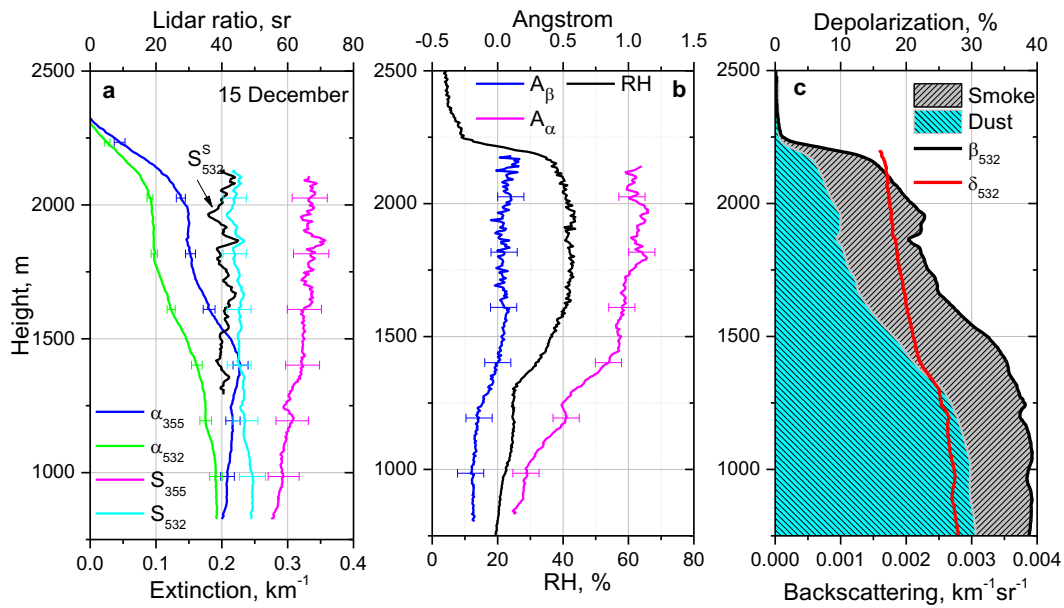
Fig.18. Vertical profiles of (a) extinction coefficients (α_{355}, α_{532}) and lidar ratios (S_{355}, S_{532}); (b) extinction, backscattering Ångström exponents (A_α, A_β) at $355 - 532$ nm and relative humidity RH; (c) contribution of dust and smoke to β_{532} together with particle depolarization ratio δ_{532} on 15 December (04:00 – 06:00 UTC). Black line in plot (a) shows the lidar ratio of smoke S^s_{532} calculated from Eq.5.

931
932
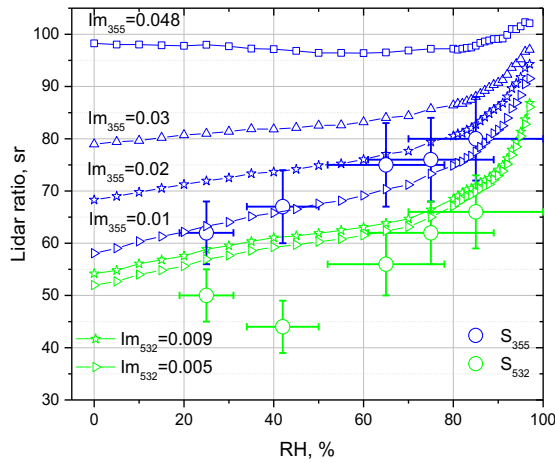
933
934 Fig.19. Modeled lidar ratios of organic carbon at 355 nm and 532 nm (line + symbol) as a function
935 of the relative humidity for the particle parameters used in the MERRA-2 model. At 355 nm results
936 are given for four values of the imaginary part of dry particles: Im_{355}= 0.048, 0.03. 0.02, 0.01. At
937 532 nm two values Im_{532}= 0.009 and 0.005 are considered. The scattered symbols (circles) show
938 the lidar ratios (S_{355}, S_{532}) observed during five smoke episodes from Table 1.
939
940